INTERNATIONAL JOURNAL OF CLIMATOLOGY
Int. J. Climatol. (2013)
Published online in Wiley Online Library
(wileyonlinelibrary.com) DOI: 10.1002/joc.3822

RMetS
Royal Meteorological Society

A CMIP5 multimodel projection of future temperature, precipitation, and climatological drought in China

Lin Wang[a,b] and Wen Chen[a]*

[a] *Center for Monsoon System Research, Institute of Atmospheric Physics, Chinese Academy of Sciences, Beijing, China*
[b] *University of Chinese Academy of Sciences, Beijing, China*

ABSTRACT: In this study, fine-resolution multimodel climate projections over China are developed based on 35 climate models and two emissions scenarios (RCP4.5 and RCP8.5) from phase five of the Coupled Model Intercomparison Project (CMIP5) by means of Bias Correction and Spatial Disaggregation. The yearly-averaged temperature is projected to increase by 0.8 to 1.6 °C (0.8 to 1.7 °C), 1.5 to 2.7 °C (2 to 3.7 °C), and 1.9 to 3.3 °C (3.4 to 6 °C) under RCP4.5 (RCP8.5) in three time slices (2010–2039, 2040–2069, and 2070–2099), respectively. The most warming occurs in winter and the least in summer, and the inland areas in the northwest will warm much faster than the southeast. Under the background of surface warming, the probability of extreme low temperatures in winter defined as the monthly temperature being lower than the 9th percentile of the climatological distribution will sharply reduce to 0.1–1.7% under RCP4.5 for the period 2010–2039 and even lower for the following decades. For precipitation change, a remarkable increase is found over most areas of China except the Southwest, ranging from approximately 2 to 20%. The projected precipitation changes are highly robust in northern China, but inconsistent in southern China. In spite of widespread precipitation increases, most areas of China quantified by the Palmer Drought Severity Index are projected to become drier as a consequence of increasing evaporation driven by temperature increases. Detailed examination shows that drought that is moderate or severe according to current climate standards will become the norm in the future. Not only will incidences of severe and extreme drought increase dramatically in the future, but extreme wet events will also become more probable. Furthermore, the increasing drought risk in Southwest China and the Qinghai-Tibetan Plateau is nearly twice that for other parts of China.

KEY WORDS climate change projection; bias correction and spatial disaggregation; Palmer Drought Severity Index; China

Received 3 February 2013; Revised 8 July 2013; Accepted 12 August 2013

1. Introduction

Nowadays, climate change is at the forefront of scientific issues and poses a significant challenge to human survival and development, especially in China. Under the background of global warming, the most noticeable climate characteristic in China since the late 19th century is the remarkable increase in temperature (e.g., Ren *et al.*, 2005; Li *et al.*, 2010b; Wei and Chen, 2011). Wang and Li (2007) showed that the correlation between the global mean temperature and the mean temperature for China is 0.63 for the last 123 years, indicating good parallelism between the warming in China and that of the world. For precipitation, prominent features include northern China becoming drier and central China becoming moister during summer and southern and east-central China becoming moister during winter (e.g., Hu *et al.*, 2003; Chen *et al.*, 2006; Zhou *et al.*, 2006; Gu *et al.*, 2009; Li *et al.*, 2009, 2010c; Liu *et al.*, 2011; Ma *et al.*, 2012; Wu *et al.*, 2012). It is also worth noting that China frequently suffers from natural disasters. Among the costliest of natural disasters, drought is a long-term phenomenon that affects large regions and inflicts significant socioeconomic and personal damage. In China, in contrast to floods, which account for only 27.8% of the total loss from meteorological disasters, the average loss resulting from drought can reach to about 50%, as in the extreme drought events in both 2006 and from autumn 2009 to spring 2010 in Southwest China (Liu, 2012). In recent decades, China has experienced rapid economic growth, but with only 7% of the world's arable land available to feed 22% of the world's population, China's economy may be vulnerable to climate change. Consequently, great effort has been expended on researching future temperature and precipitation change in China in order to serve economic and social development. Previously, analyses of the projected variation in temperature and precipitation in China depended mainly on phase three of the Coupled Model Intercomparison Project (CMIP3; Zhou and Yu, 2006; Feng *et al.*, 2011). Up to the present, however, phase five of the Coupled Model Intercomparison Project (CMIP5) has been carried out with a new set of coordinated climate model experiments (Taylor *et al.*, 2012). Moreover, the publication of the Fifth Assessment Report (AR5) from the Intergovernmental Panel on Climate Change (IPCC) is scheduled for late 2013. The key factors of

* Correspondence to: W. Chen, Institute of Atmospheric Physics, Chinese Academy of Sciences, P.O. Box 2718, Beijing 100190, China. E-mail: cw@post.iap.ac.cn

AR5 involve an understanding of climate change in the past 100 years and projections for the next 100 years. Therefore, it is of paramount importance to assess future changes in temperature, precipitation and climatological drought over China under the CMIP5 framework.

Though coupled general circulation models (GCMs), which describe oceanic and atmospheric dynamical processes, are the primary tools for studying global climate change, it is well known that global climate models have a typical resolution of a few hundred kilometres. Thus, their resolution is too coarse to provide the regional-scale information required for regional impact assessment. Consequently, it is necessary to bridge the gap between the coarse resolution of current GCMs and the level of detail desired at regional or local scales. Downscaling techniques are commonly used to obtain regional or local future climate scenarios. Two downscaling approaches can be identified: dynamical downscaling (high-resolution regional models nested in GCMs; Giorgi and Mearns, 1991) and statistical downscaling (statistical relationship between large-scale atmospheric variables and regional or local climate variables; Wilby and Wigley, 1997). A number of studies have compared the relative strengths and weaknesses of these two downscaling techniques. Dynamical downscaling is implemented using a fine-scale regional climate model (RCM) with a better representation of local terrain that simulates climate processes over the region of interest. On the other hand, statistical downscaling is based on a stable climate rather than physical processes. Dynamical downscaling is computationally expensive, but it is feasible to perform downscaling for a large number of simulations with multiple GCM configurations and emissions scenarios by using a statistical approach that is computationally efficient.

In parallel, in addition to the inappropriate scale of most regional impact analyses derived from GCMs, GCM outputs also suffer from biases due to uncertainty in the parameterization of unresolved processes. While large or global-scale patterns of temperature and precipitation simulated by state-of-the-art GCMs can be realistic (Solomon *et al.*, 2007), biases at the regional scale may be large enough to negatively affect regional climate assessment (Kunkel *et al.*, 2006). Therefore, it is crucial that GCM simulations be bias corrected in order to draw valid conclusions in regional climate impact and vulnerability assessment. The importance of bias correction was described in a special IPCC report (Seneviratne *et al.*, 2012). To cope with the large biases in GCMs, many techniques have been utilized to post-process the raw GCM output, such as monthly mean correction (Fowler and Kilsby, 2007), delta change (Hay *et al.*, 2000) and quantile mapping (Wood *et al.*, 2002). Among these methods, the most popular is quantile mapping, which adjusts the distribution of the model output to match all statistical moments with respect to observations.

One technique that solves the abovementioned problems is the Bias Correction and Spatial Disaggregation (BCSD) approach originally developed by Wood *et al.* (2002, 2004). The BCSD method has been shown to provide downscaling capabilities comparable to other statistical and dynamical methods (Wood *et al.*, 2004). Using GCM precipitation as a predictor, on the one hand, makes it possible to capture the complexity of physical processes which cannot be achieved by using only larger-scale circulation indicators (Maurer and Hidalgo, 2008). On the other hand, Widmann *et al.* (2003) noted that using local predictors such as precipitation yielded a performance comparable with other downscaling methods. This method has been widely used recently in regional climate impact assessment. Sharma *et al.* (2007) utilized BCSD to correct and downscale GCM precipitation to improve hydrological simulation in the Ping River Basin, Thailand. Based on a variant of BCSD called Bias-corrected Local Scaling, Vidal and Wade (2008a) developed a multimodel high-resolution climate projection for the United Kingdom in the 21st century and performed a detailed assessment of future climatological drought patterns (Vidal and Wade, 2009). Piani *et al.* (2010) validated the bias correction method for daily precipitation over Europe, showing that this method performs well in all moments of the probability density distribution. Maurer *et al.* (2007) developed a dataset of fine-resolution climate projections using BCSD based on CMIP3 multimodel dataset (Meehl *et al.*, 2007). This globally downscaled dataset facilitates regional climate impact studies.

More recently, researchers have been analysing future projections in China based on CMIP5 model outputs. Xu and Xu (2012) described temperature and precipitation changes over China using 11 climate projections. Zhang (2012) employed 17 models out of CMIP5 to investigate the temporal and spatial characteristics of 2 $^{\circ}$C warming over China under RCP4.5. However, these studies did not perform bias correction and spatial downscaling, the importance of which was described above. In addition, merely a small subset of the CMIP5 data repository was used to generate a multimodel ensemble mean in these studies. Moreover, for multimodel ensembles, the arithmetic mean was used in all these studies. However, developing multimodel ensemble means requires considering the various strengths and weaknesses of each individual model. The key question is how to build climate projections for a set of global circulation models (GCMs). Many different techniques have been developed, such as the reliability average ensemble proposed by Giorgi and Mearns (2002) and Bayesian methodology (Furrer *et al.*, 2007). However, instead of introducing a model weighting scheme based on how well each model reproduces the current climate, the bias-correction step in BCSD allows us to assign the same weight to each individual projection (Vidal and Wade, 2008b). In addition, the change in drought, which is of great concern in the changing climate, is not well documented. Precipitation alone is not a good indicator of drought, because drought also depends on the trend and fluctuation of temperature due to its influence on evapotranspiration.

In this study, BCSD is first implemented in order to increase confidence in examining future changes. This paper is structured as follows: Section 2 presents the

data, including the observations and the models used. In Section 3, we describe the BCSD technique. The performances of the models' simulations over China are assessed in Section 4. Future changes in temperature and precipitation are assessed in Sections 5. Section 6 shows the results of the projected change in climatological drought. Finally, conclusions are presented in Section 7.

2. Data

The observed temperature (°C) and precipitation (mm month^{-1}) used in this study are gridded data on a 0.5° latitude–longitude resolution elaborated by the China Meteorological Administration. These datasets cover the time period from 1961 to 2005 in monthly time intervals. The observational data are confined to mainland China because of the unavailability of data from Taiwan.

To assess potential future changes in temperature, precipitation, and climatological drought, monthly outputs from 35 GCMs are extracted from CMIP5. The projection data are archived by the Program for Climate Model Diagnosis and Intercomparison (PCMDI). The two 21st-century scenarios for future greenhouse gas emissions used in this study are RCP4.5 and RCP8.5 as defined in Moss *et al.* (2010), where RCP8.5 is a higher emission path and RCP4.5 assumes lower emissions. Monthly mean surface temperatures and precipitation from simulations of a historical run, an RCP4.5 run, and an RCP8.5 run are used in this study. Though the historical run covers the period from the mid-19th century to 2005, the data from 1961 to 2005 are extracted owing to the availability of observation data. In addition, only one ensemble member from each model is chosen for this study, though multiple ensemble members are generally accessible. Table 1 lists the basic information about the models, the associated institution, and the resolution of the atmospheric component. In this study, we consider 1961–1990 to be the reference period recommended by WMO (2007) and also consider three additional time intervals of 30 years, 2010–2039 (the beginning-of-century), 2040–2069 (the mid-century), and 2070–2099 (the end-of-century). Accordingly, results from temperature, precipitation, and the Palmer Drought Severity Index (PDSI) are analysed and displayed for these three time slices.

3. Methodology

Bias correction and spatial disaggregation relies on finer-scale observation data and consists of the following steps: (1) aggregate finer-scale observed data to a GCM-specific scale; (2) correct the GCM's systematic biases through quantile mapping; and (3) disaggregate bias-corrected outputs to a finer scale.

3.1. Quantile mapping

The principle of quantile mapping is to adjust the distribution of the model outputs so it closely resembles the observed climatology by finding a transfer function between the model outputs and the observations. This method can be generally formulated as (Gudmundsson *et al.*, 2012):

$$\widetilde{x}_{adjst} = h\,(x) \tag{1}$$

where h is the transfer function established between model outputs and observations in the reference period and x is the climate variable in either the reference or a projection period. Furthermore, if the theoretical distribution of the variable of interest is known, expression 1 can be written as (Gudmundsson *et al.*, 2012):

$$\widetilde{x}_{adjst} = F_{o-c}^{-1} \cdot F_{m-c}\,(x) \tag{2}$$

where F_{o-c}^{-1} is the quantile function corresponding to observations and F_{m-c} is the cumulative distribution function (CDF) of model outputs in the reference period.

The basic assumption of traditional quantile mapping is that the future distribution of a variable of interest will remain similar to that in the reference period. However, this may not hold true, as argued by Li *et al.* (2010a), who recently proposed a new quantile-based mapping method called equidistant cumulative distribution function matching (EDCDFm) as an improvement over the traditional CDF matching method. This method explicitly takes into account the changes between the reference and future distributions for a specific model. This improved quantile mapping method can be mathematically written as:

$$\begin{aligned}\widetilde{x}_{m-p.adjst} = x_{m-p} &+ F_{o-c}^{-1}\left(F_{m-p}\left(x_{m-p}\right)\right) \\ &- F_{m-c}^{-1}\left(F_{m-p}\left(x_{m-p}\right)\right)\end{aligned} \tag{3}$$

where F_{m-p} is the CDF of the model for a future projection period, and F_{o-c}^{-1} and F_{m-c}^{-1} are quantile functions for observations and model in the reference period, respectively. Though this method incorporates the distribution change, the underlying assumption is that the difference between the model and the observed values during the reference period will remain stationary in a future period. By performing a synthetic experiment, Li *et al.* (2010a) concluded that the EDCDFm method is superior to the traditional method.

However, the EDCDFm method has some shortcomings when applied to bias-correct precipitation. It is evident that all terms on the right side of expression (3) are positive. However, we cannot guarantee the positivity of the resultant value, the model precipitation after bias correction in a future period. We have used this exact same method on CMIP5 precipitation data and found that this situation does exist. Since the validation in Li *et al.* (2010a) focused mainly on the climatological field, the negative values of precipitation were covered up by long-term means.

The term $F_{o-c}^{-1}\left(F_{m-p}\left(x_{m-p}\right)\right) - F_{m-c}^{-1}\left(F_{m-p}\left(x_{m-p}\right)\right)$ on the right side of expression (3) can be called 'quantile mapping factors'. For temperature, this works well and can be further designated the 'additive factor'. For precipitation, in order to avoid the problem of a negative value as a result of

Table 1. Summary of 35 general circulation models from CMIP5 used for this study.

Model acronym	Modelling center	Atmospheric component resolution(Lon × Lat)
ACCESS1-0	Commonwealth Scientific and Industrial Research Organization (CSIRO) and Bureau of Meteorology (BOM), Australia	1.875° × 1.25°
ACCESS1-3		
bcc-csm1-1	Beijing Climate Center, China Meteorological Administration, China	∼2.8° × 2.8°
BNU-ESM	College of Global Change and Earth System Science, Beijing Normal University, China	∼2.8° × 2.8°
CanESM2	Canadian Centre for Climate Modelling and Analysis, Canada	∼2.8° × 2.8°
CCSM4	National Center for Atmospheric Research, USA	1.25° × 0.9°
CESM1-BGC	Community Earth System Model Contributors, USA	1.25° × 0.9°
CESM1-CAM5		1.25° × 0.9°
CESM1-WACCM		2.5° × 1.9°
CMCC-CM	Centro Euro-Mediterraneo per I Cambiamenti Climatici, Italy	∼0.75° × 0.75°
CNRM-CM5	Centre National de Recherches Météorologiques/Centre Européen de Recherche et Formation Avancées en Calcul Scientifique, France	∼1.4° × 1.4°
CSIRO-Mk-3-6-0	Commonwealth Scientific and Industrial Research Organization in collaboration with the Queensland Climate Change Centre of Excellence, Australia	1.875° × 1.875°
EC-EARTH	EC-EARTH consortium, Europe	1.125° × 1.125°
FGOALS-g2	LASG, Institute of Atmospheric Physics, Chinese Academy of Sciences and CESS, Tsinghua University, China	2.8125° × 3°
FGOALS-s2	LASG, Institute of Atmospheric Physics, Chinese Academy of Sciences, China	∼2.81° × 1.66°
FIO-ESM	The First Institution of Oceanography, SOA, China	∼2.8° × 2.8°
GFDL-CM3	NOAA Geophysical Fluid Dynamics Laboratory, USA	2.5° × 2°
GFDL-ESM2G		2.5° × 2°
GFDL-ESM2M		2.5° × 2°
GISS-E2-H	NASA Goddard Institute for Space Studies, USA	2.5° × 2°
GISS-E2-R		2.5° × 2°
HadGEM2-CC	Met Office Hadley Centre (additional HadGEM2-ES realizations contributed by Instituto Nacional de Pesquisas Espaciais), United Kingdom	1.875° × 1.25°
HadGEM2-ES		1.875° × 1.25°
HadGEM2-AO	National Institute of Meteorological Research/Korea Meteorological Administration, Korea	1.875° × 1.25°
inmcm4	Institute for Numerical Mathematics, Russia	2° × 1.5°
IPSL-CM5A-LR	Institut Pierre-Simon Laplace, France	3.75° × 1.875°
IPSL-CM5A-MR		2.5° × 1.25°
IPSL-CM5B-LR		3.75° × 1.875°
MIROC5	Atmosphere and Ocean Research Institute (The University of Tokyo), National Institute for Environmental Studies, and Japan Agency for Marine-Earth Science and Technology, Japan	∼1.4° × 1.4°
MIROC-ESM	Japan Agency for Marine-Earth Science and Technology, Atmosphere and Ocean Research Institute (The University of Tokyo), and National Institute for Environmental Studies, Japan	∼2.8° × 2.8°
MIROC-ESM-CHEM		∼2.8° × 2.8°
MPI-ESM-LR	Max-Planck-Institut für Meteorologie (Max Planck Institute for Meteorology), Germany	1.875° × 1.875°
MPI-ESM-MR		1.875° × 1.875°
MRI-CGCM3	Meteorological Research Institute, Japan	1.125° × 1.125°
NorESM1-M	Norwegian Climate Centre, Norway	2.5° × 1.875°

applying the additive factor, the multiplicative factor $F_{o-c}^{-1}\left(F_{m-p}\left(x_{m-p}\right)\right)/F_{m-c}^{-1}\left(F_{m-p}\left(x_{m-p}\right)\right)$ can be used. The underlying assumption of the multiplicative scaling factor is that the ratio between the observed and modelled values during the reference period also applies to the projection period. Consequently, this method can be referred to as equiratio cumulative distribution function matching (equiratio CDFm). A real-world assessment based on an ensemble of GCMs from CMIP5 confirms the effectiveness and robustness of equiratio CDF matching in systematically removing biases in modelled precipitations (Wang and Chen, 2013). The statistical transformation can be written as:

$$\widetilde{x}_{m-p.adjst} = x_{m-p} \cdot \frac{F_{o-c}^{-1}\left(F_{m-p}\left(x_{m-p}\right)\right)}{F_{m-c}^{-1}\left(F_{m-p}\left(x_{m-p}\right)\right)}. \quad (4)$$

Subsequently, another important step is how to estimate the transfer function. Gudmundsson *et al.* (2012) have recently summarized methods of statistical transformation and have classified them into three categories: (1) distribution-derived transformations, (2) parametric transformations, and (3) nonparametric transformations. Nonparametric transformation is recommended by Gudmundsson *et al.* (2012) for most applications of statistical transformation, since it can be applied without specific

assumptions about the distribution of the observed or modelled data. Consequently, the quantile mapping method used in this study can be formulated as:

$$\begin{aligned} \widetilde{x}_{m-p.adjst} &= x_{m-p} + h1\left(x_{m-p}\right) \\ &\quad -h2(x_{m-p}) \quad \text{for temperature} \\ \widetilde{x}_{m-p.adjst} &= x_{m-p} \cdot \frac{h1(x_{m-p})}{h2(x_{m-p})} \quad \text{for precipitation.} \end{aligned} \tag{5}$$

In Equation (5), two transfer functions are constructed: they represent the mapping from the quantiles of the model in the projection period to (1) those of the observation in the reference period, $h1$, and (2) those of the model in the reference period, $h2$. These two transfer functions are determined separately for each calendar month, grid point, and variable and once again the bias correction procedures are conducted after observations being aggregated to the GCM-specific scale. Technically, in the case of $h1 = F_{o-c}^{-1} \cdot F_{m-p}$, the transfer function is derived in the following steps: (1) sort the time series by intensity for both the observations in the reference period and the modelled values in a future projection period which have the same sample size of 30 in this study, and plot the quantile–quantile correspondence between two time series; (2) make use of cubic smoothing splines, one of nonparametric approaches, to fit the established quantile–quantile plot and then obtain the smoothing parameters. Because the cubic smoothing splines extend beyond the range of training values, no additional extrapolation is needed to treat the out-of-range new values specially. Nevertheless, it is well known that frequent extrapolations will introduce large uncertainties in resulting bias-corrected values. Actually, the proposed bias-correction procedure in this study requires little extrapolation, which can be identified as another advantage over the traditional quantile mapping. The traditional method can be mathematically formulated as $\widetilde{x}_{adjst} = F_{o-c}^{-1} \cdot F_{m-c}\,(x)$, in which F_{m-c} is determined by the values in the reference period. As we know, however, there may be a significant long-term trend for temperature. Therefore, extrapolation is frequently required to obtain $F_{m-c}(x_p)$, since most of the future temperature would be outside of the present range. But this is not the case for the improved method proposed in this study. For the equidistant or equiratio CDF matching (see Equations 3 and (4)), the value $F_{m-p}(x_p)$ is calculated instead of $F_{m-c}(x_p)$, so there is no need to do extrapolation since the x_p is definitely within the range of F_{m-p}. For the same reason, no extrapolation is required to estimate $F_{o-c}^{-1}\left(F_{m-p}\left(x_{m-p}\right)\right)$ and $F_{m-c}^{-1}\left(F_{m-p}\left(x_{m-p}\right)\right)$.

3.2. Spatial disaggregation

Following bias correction, the monthly GCM-scale fields are then downscaled to $0.5^\circ \times 0.5^\circ$ resolution. The detailed process of spatial disaggregation is illustrated in Figure 1, in which the raw modelled temperature from IPSL-CM5A-LR in July 1985 is downscaled to the finer grid scale, identical with that of observation. The reason for choosing IPSL-CM5A-LR as an example is its lowest resolution among all GCMs, which may enhance the visual effect of downscaling. First, the observed climatological temperatures in July for the baseline period are calculated (Figure 1(a)) and then aggregated to the GCM-specific grid scale (Figure 1(b)). Second, the factors (also called anomalies) exemplified in Figure 1(d) are obtained by subtracting the coarse-scale observed monthly means (Figure 1(b)) from the bias-corrected GCM outputs (Figure 1(c), 'GCM outputs' for short hereafter in this subsection). For precipitation, the ratios of GCM outputs to climatological observations after aggregation are computed to create factor fields, in order to avoid negative precipitation values. Third, the factors are spatially bilinear-interpolated to the resolution ($0.5^\circ \times 0.5^\circ$) of observation (Figure 1(e)). Finally, the coarse-scale GCM outputs are translated to the finer scale (Figure 1(f)): the factor fields having been subjected to interpolation step (Figure 1(e)) are summed with observed means in original scale (Figure 1(a)). For precipitation, to generate the finer spatial pattern, the interpolated factors are multiplied by the observed fine scale means.

It is necessary to stress that, though in this study we focus on region- or nation-wide results, spatial disaggregation process is inevitably crucial to construct multimodel ensemble mean. As we know, different models have different horizontal resolutions. Consequently, the most troublesome issue is how to unify the horizontal resolution among different GCMs. We can interpolate each model output field linearly to a prescribed grid. Nevertheless, which is the best way to objectively choose a suitable target grid? Here, the spatial disaggregation is a good choice.

3.3. PDSI as a drought index

To quantify drought severity and spatial distribution, the PDSI is employed here. This index is a landmark in the development of drought indices. The PDSI was created by Palmer (1965), based on the supply and demand of the two-stage 'bucket' model of soil. The prominent advantage of PDSI is its sensitivity to changes in evapotranspiration demand caused by temperature fluctuations and trends (Dai, 2011). Moreover, in contrast to other statistically based drought indices, the PDSI is based on a physical water-balance model. However, major deficiencies of the PDSI include high sensitivity to the calibration period and spatial incomparability (Alley, 1984). Wells *et al.* (2004), who developed the self-calibrating PDSI, solved most of the PDSI's calibration problems. The classification of droughts according to PDSI is shown in Table 2.

Potential evapotranspiration (PET), one of the inputs to the PDSI, is estimated here following Thornthwaite (1948). However, there are concerns that the Thornthwaite method may overestimate PET (Hobbins *et al.*, 2008; van der Schrier *et al.*, 2011), especially in the tropics. This overestimation is closely associated with the exclusion of cloud cover and vapour pressure deficit in the parameterization of Thornthwaite. On the other hand, the Penman-Monteith approach (Allen *et al.*, 1994), recommended by the Food and Agricultural Organization

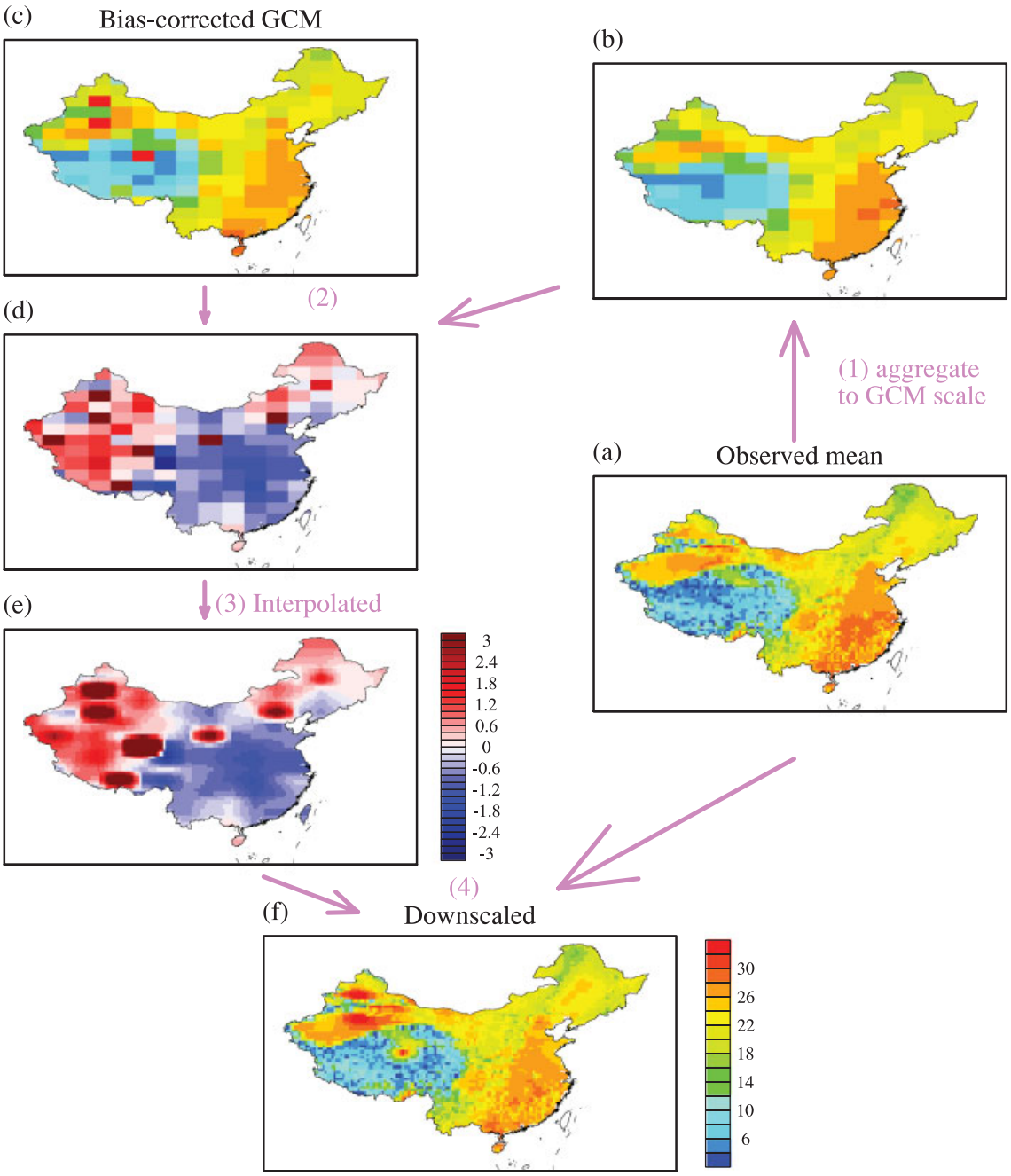

Figure 1. Schematic illustration of the spatial disaggregation process. The downscaled temperature field is constructed from bias-corrected IPSL-CM5A-LR values for July 1985.

(FAO), is thought to give a more realistic estimate of PET. However, it requires additional input fields including solar radiation, wind speed, cloudiness, and humidity, which make the calculations and evaluation more complicated. Though model outputs comprise these fields, there are no adequate observational data of these variables for bias correction. Several previous studies (Dai, 2011; van der Schrier *et al.*, 2011) have demonstrated that the choice of PET parameterization method has a limited effect on the PDSI in the present climate. However, this may not be the case in the future changing climate and several recent studies pointed out that PET change is highly dependent on parameterization scheme (Shaw and Riha, 2011; Prudhomme and Williamson, 2013). It is necessary to stress that different formulation of PET may lead to different results, which requires further studies.

In this article, the self-calibrating PDSI is calculated instead of the original PDSI. For simplicity, the self-calibrating PDSI is referred to as PDSI hereafter. The Thornthwaite method is utilized here and the calibration period is from 1961 to 1990. For water-holding capacity, we use a soil texture-derived water-holding capacity map at $1^\circ \times 1^\circ$ resolutions from Webb *et al.* (1993). The

Table 2. Classification of PDSI values.

PDSI value	PDSI category
≥4.0	Extremely wet
3.00 to 3.99	Very wet
2.00 to 2.99	Moderately wet
1.00 to 1.99	Slightly wet
0.50 to 0.99	Incipient wet
0.49 to −0.49	Near normal
−0.50 to −0.99	Incipient drought
−1.00 to −1.99	Mild drought
−2.00 to −2.99	Moderate drought
−3.00 to −3.99	Severe drought
≤−4.0	Extreme drought

data are first interpolated via a bilinear method to the temperature or precipitation grid prior to computation of the PDSI. Once again, the temperature and precipitation after BCSD, rather than the original data, are used for the PDSI calculation.

3.4. Climate divisions of China

Because China covers a large area with complex topography and diverse climate zones, it is necessary to define climate divisions in order to study the regional disparity in climate change. Considering regional climate characteristics and also taking into account administrative divisions, China is classified into seven climate regions according to Wang and Li (2007, Figure 3.3), namely Northeast China (NE), North China (N), Northwest China (NW), East China (E), Southwest China (SW), Qinghai-Tibetan Plateau (QT), and South China (S). Figure 2 shows a map of China's terrain and seven climate divisions.

4. Model biases

This section discusses a preliminary investigation of GCM performance over China. Though many coupled models that include major greenhouse gases and sulphate aerosols are able to reproduce major trends in global average surface air temperature, considerable systematic errors may still exist at regional scales. In this study, the average model-performance error is quantified by the mean absolute error (MAE), which is a more natural measure of average error than the root-mean-square error (Willmott and Matsuura, 2005). This accuracy estimator can be mathematically written as:

$$\mathrm{MAE} = N^{-1}\sum_{i=1}^{N}|P_i - O_i| \tag{6}$$

where P_i and O_i are the model estimate and the observed value, respectively for a specific grid cell, and N is the total number of grid cells within China for a given model.

Figure 3(a) shows the MAE between the simulated and observed monthly mean temperature for each model and calendar month. With a few exceptions, the MAEs are widespread over more than 2 °C, with the largest bias being 5.7 °C. The percentages of MAE greater than 2 °C and 3 °C account for 83 and 34%, respectively, indicating that most models could not accurately recreate the observed climatology for temperature at a regional scale (here in China). For the seasonal cycle, the simulated temperature in warm seasons is better than that in cool seasons since the medians in January and July are 3.1 °C and 2.3 °C, respectively. Overall, the model EC-EARTH has the highest skill in reproducing the climatological temperature over China, which is also the case for precipitation simulation as discussed below.

Figure 3(b) shows that the biases of precipitation quantified by the MAE are much larger in summer than in winter, about 60 mm *versus* 20 mm in terms of median. Relatively large biases are noticeable in the summer half of the year, with the largest MAE being more than 80 mm. If we inspect the percentage error instead of absolute error, however, the largest biases occur in dry season due to low climatological precipitation. Furthermore, it is very common for percentage error to exceed 100% with the largest reaching up 1600% during dry season.

It is worth noting that the main purpose here is to quantify the magnitude of model errors regardless of cold or warm biases (for precipitation, dry biased or wet biased). Figures showing the spatial distributions of biases are omitted here due to the large number of individual simulations, but we found that large biases exist in various models. Furthermore, there are significant systematic errors in monthly higher-order statistics (i.e., variance and skewness) of both temperature and precipitation when compared to observations. In addition, we do not intend to rank each model according to its performance but to illustrate the enormous systematic errors inherent in GCMs. Obviously, current GCMs still have substantial deficiencies in simulating the regional climate over China. To produce the reliable projections required for regional climate assessment, we need to bias-correct the raw GCM outputs.

5. Projected changes in temperature and precipitation

5.1. Changes in the mean temperature

For a given time period (2010 to 2039, 2040 to 2069, or 2070 to 2099) and emission scenario (RCP4.5 or RCP8.5), projections from different GCMs are considered equally plausible in the representation of future climate, and subsequently the multimodel ensemble is built through the arithmetic mean. In this section, we first analyse the projected changes in temperature and then precipitation. Because the projected changes to a variable of interest differ among various GCM runs, a ratio of the same sign is employed here to quantify this kind of uncertainty. Hereafter, changes in temperature, precipitation, and PDSI from the reference period (1961–1990) to the projection period (2010 to 2039, 2040 to 2069,

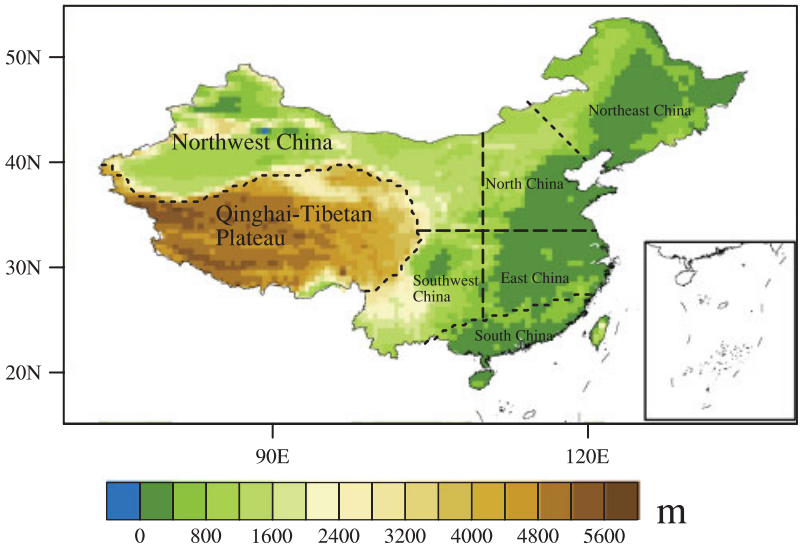

Figure 2. China's terrain and distribution of seven climate divisions.

or 2070 to 2099) are denoted as ΔT, ΔP, and $\Delta PDSI$, respectively.

The projected changes in national average temperatures from all GCM runs are portrayed by boxplots in Figure 4. National average temperatures are expected to increase by 1.0–1.3 °C, 2.0–2.5 °C, and 2.4–3° C, depending on the calendar month, for the beginning, middle, and end of the 21st century, respectively, under RCP4.5 on the basis of multimodel medians. The seasonal signature is pronounced in surface warming, with the greatest warming in the wintertime and the least in the summertime, especially in the period of 2070–2099. The boxplots in Figure 4 measure the model dispersion through five statistics: sample minimum, lower quartile, median, upper quartile, and sample maximum. Obviously, the dispersion described by the maximum minus minimum increases steadily from 1 to 4 °C under RCP4.5 from the beginning to the end of the 21st century, which implies the inter-model dispersion tends to broaden with time for all calendar months, reflecting the increase in uncertainty when we move further into the future. Additionally, for the minimum to maximum range of GCM-projected temperature change, there is no substantial variation with respect to the seasonal cycle. For the period 2010–2039 (Figure 4(a) and (b)), the magnitudes of temperature increase for RCP4.5 and RCP8.5 are similar due to the small difference between the two emission pathways before 2050. As a result of the rising radiative forcing pathway leading to 8.5 W m^{-2} by 2100 for scenario RCP8.5, the climatological temperature begins to show vastly different features after the mid-century. The monthly temperature increase can reach 4–6 °C under RCP8.5, but only about 2–4 °C under RCP4.5 for the end-of-century.

Geographic distributions of projected changes in climatological annual temperature are shown in Figure 5. The models project widespread temperature increases across the whole country, with the largest increase in winter (figure not shown), which closely resembles the seasonality of the national mean temperature increase illustrated in Figure 4. For a given future period and emission scenario, though warming is found in all regions of China, larger relative increases are projected for inland regions, especially the Northwest, with a relatively small increase in coastal regions, perhaps due to the ocean's moderating influence. When considering the beginning-of-century, the different emission scenarios do not lead to dramatically different temperature responses since the MAE between the two fields in subplots (a) and (b) of Figure 5 is only 0.12 °C. Nevertheless, for the time period 2070–2099, changes under RCP8.5 scenario are more pronounced than under RCP4.5, since the MAE is 2.3 °C. Besides, the mid-century can be viewed as a transition period during which the different temperature responses under lower and higher emissions scenarios become increasingly noticeable. Additionally, compared to the period 2010–2039, the percentage of areas in which $\Delta T > 2$ °C will prevail in the mid- and end-of-century under both emissions scenarios.

5.2. Changes in the distribution of winter temperature

Though the temporal-averaged temperature undoubtedly will increase in the 21st century, the coldest winter in the reference period may still be experienced in the future climate. Supposing that temperature series are normally distributed, if the mean shifts to the right and the variance also becomes greater as time progresses, there is still a remarkable probability of an extremely cold winter. For example, massive snowstorms hit China from 9 January to 25 February in 2008, resulting in transportation disruption, infrastructure damage, and higher food prices, among other problems (e.g., Chen *et al.*, 2008; Zhou *et al.*, 2009, 2010). Consequently, higher mean temperatures under global warming do not necessarily indicate a decreasing incidence of extreme low temperatures. In order to assess the change in probability of

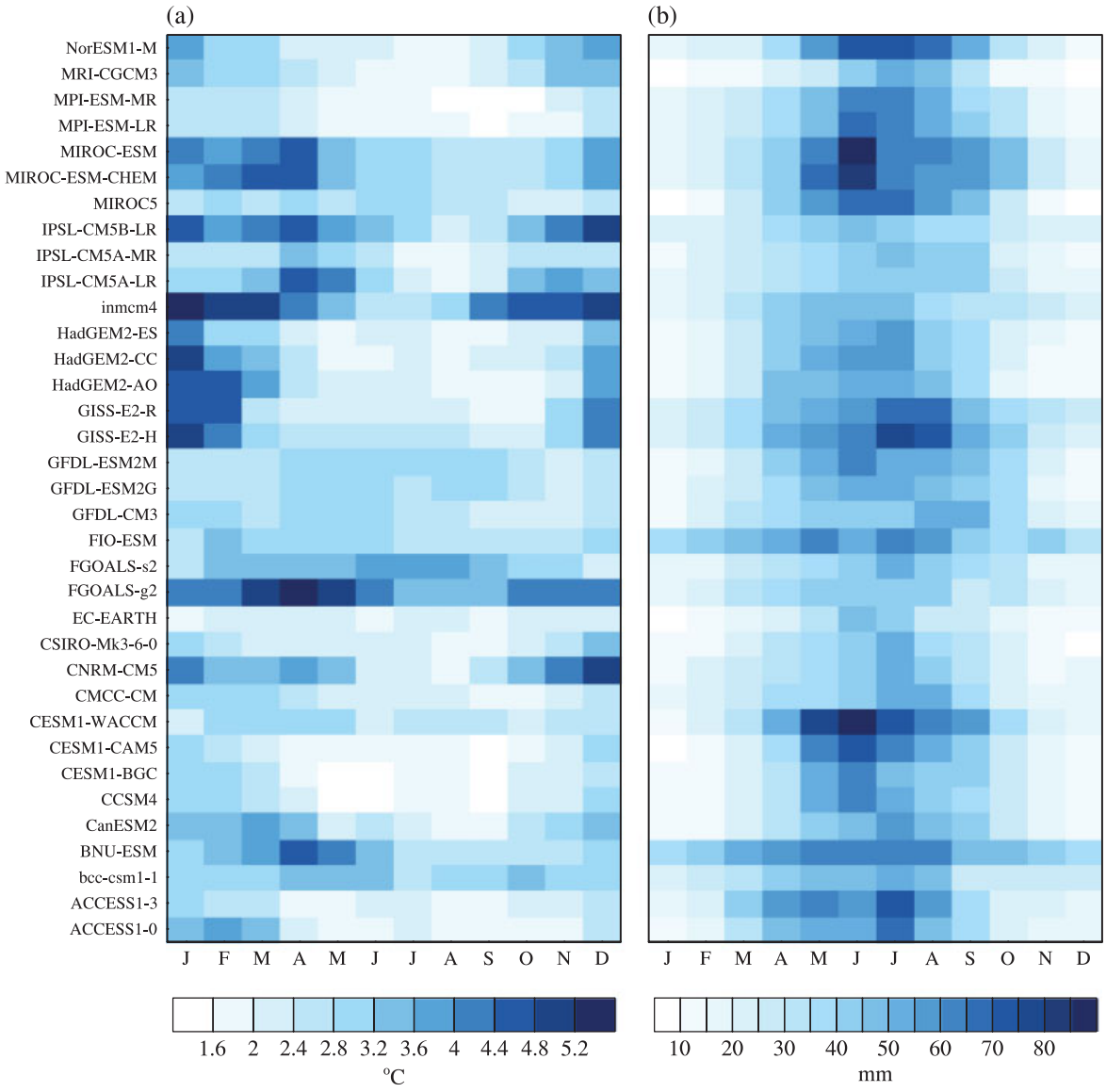

Figure 3. Biases of (a) simulated climatological monthly mean temperature (°C) and precipitation (mm) expressed in mean absolute error during the reference period for each calendar month and individual model. Colour intensities reflect the magnitude of the biases. x- and y-axis correspond to calendar months and GCMs, respectively.

extreme cold events in the future, a mapping between the future under RCP4.5 and historic percentiles is shown in Figure 6. The blue curve in each subplot is below the diagonal line, implying that the distribution shifts to higher temperatures. Also, the distance between the blue curve and the $X = Y$ line is broadened toward the end of the 21st century. It is worth noting the starting and ending points of the blue curve. At the beginning-of-century, the percentile–percentile curves over most climate regions (except the Qinghai-Tibetan Plateau) start at (0, 0), which means that the coldest winter temperature in the reference period will still appear in the future. Relative to the current climate, however, the probability of extreme low temperatures will decrease dramatically in this time slice. If we define the 9th percentile of the climatological distribution in the reference period as the threshold, the probability of such events will reduce to 0.9, 1.8, 1.9, 1.3, 0.6, 0.2, and 1.6% for each climate region (NE, N, NW, E, SW, QT, and S), respectively. Especially for the Qinghai-Tibetan Plateau, the lowest temperature recorded in the reference period will disappear in the beginning-of-century since the starting point of the blue curve is not at the origin. As a transition period, during the mid-century the blue lines (second row in Figure 6) representing correspondence between percentiles of winter temperature in the reference and the future period tend to deviate from the diagonal (dash–dot line). As time goes on, the pronounced gap between the ending point of the blue curve and the $X = Y$ line for the period 2070–2099 indicates that the warmest winters in the future are completely outside the range of the current distribution and the warmest winter temperature found in the current climate is ranked only in the 40–70th percentile in the NE, N, NW, E, and S and in

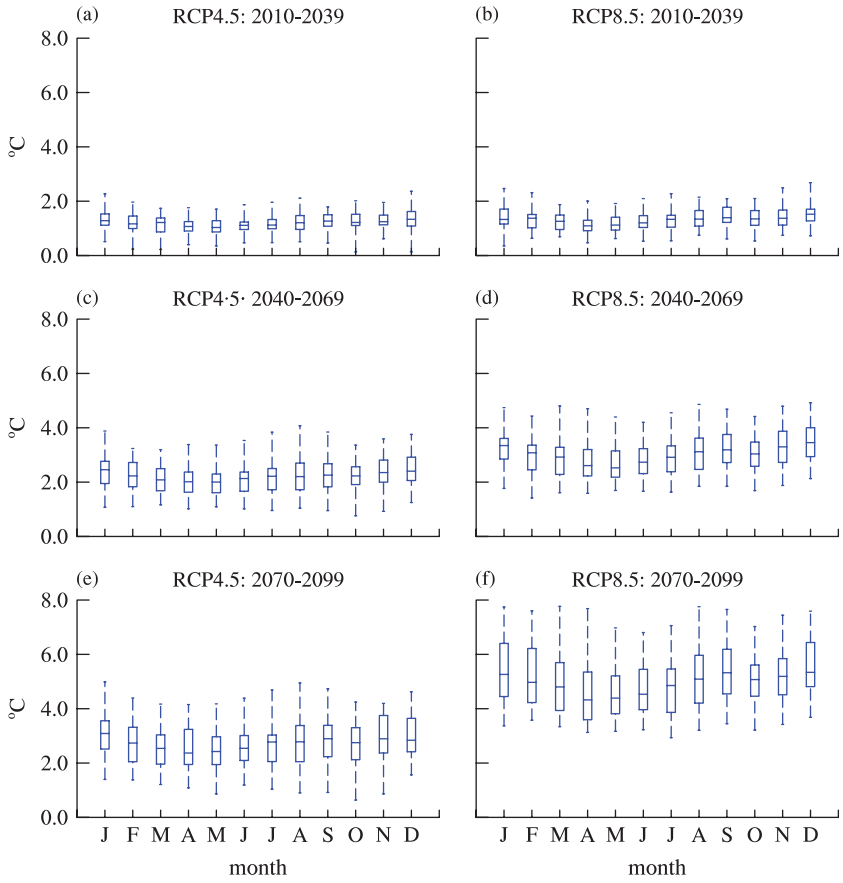

Figure 4. Projected changes in national average temperature for each calendar month from the reference period (1961–1990) to (a, b) 2010–2039 (top row), (c, d) 2040–2069 (middle row), and (e, f) 2070–2099 (bottom row) under two emissions scenarios (columns), showing all model results by means of boxplots. The band near the middle of the box shows the median and the bottom and top of the central rectangle spans the first quartile to the third quartile. Whiskers above and below the box show the location of the maximum and minimum.

the 20–30th percentile in the SW and QT. In contrast, for the period 2010–2039, the percentiles corresponding to the warmest temperature recorded during the reference period in all climate divisions range from 86th to 98th percentile. In addition, the median in the reference period is less than the 4th percentile over all regions for the end-of-century, indicating that the current normal temperature will become relatively cool compared to future climate standard.

5.3. Changes in mean precipitation

Figure 7 displays the changes in climatological monthly precipitation, averaged across China, for the periods 2010–2039, 2040–2069, and 2070–2099 under two emissions scenarios. In any time slices, results from the multimodel medians suggest an increase in precipitation for all seasons, with no significant differences between the two scenarios. The magnitude of the increase peaks in summertime, with the smallest change in wintertime. Also, seasonal differences in ΔP tend to become significant toward the late 21st century. Because China is under dry conditions from October to March due to the influence of the winter monsoon (Chen *et al.*, 2005; Zhou *et al.*, 2007), and the summer monsoon prevails from June to August (Huang *et al.*, 2003), when precipitation is plentiful, the seasonality of precipitation in the future will become slightly stronger. In terms of the minimum to maximum range, the intermodel dispersion increases by approximately 10 mm from the beginning to the end of century, with a month-to-month range from 2.7 to 31.9 mm under RCP4.5. However, the interquartile range increases only slightly, by about 2.3 mm, with a high value of 8.4 mm. The uncertainties in the projections have a marked seasonal signature with high intermodel dispersion in the rainy season. Unlike temperature, ΔP is not expected to have a consistent change in sign among all the GCM runs. However, the majority (approximately 75%) of GCMs show increases in precipitation.

To further investigate the spatial pattern of precipitation changes, Figure 8 maps the multimodel averaged results and gives the uncertainty in each grid cell. At the beginning-of-century, the projected changes are rather mixed, with a decrease in precipitation in Southwest China and an increase in other parts of China. A remarkable increase of up to 5–10% is found in Northwest China, Northeast China, and North China, where the changes are coherent between the different model projections. Moreover, the magnitude of the precipitation increase under RCP8.5 in these regions is slightly larger than that under RCP4.5. It is evident in Figure 8(a)

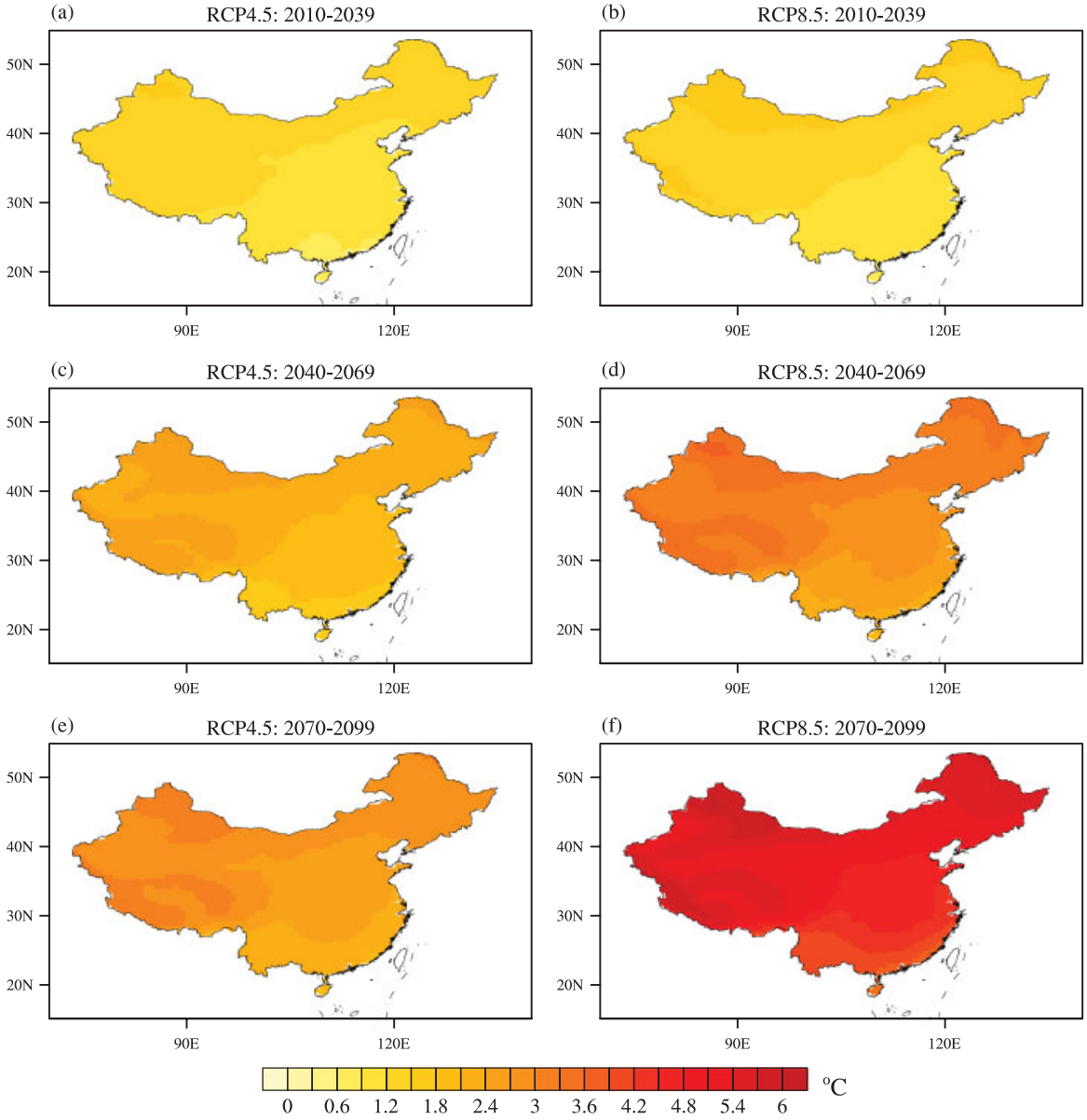

Figure 5. Geographic distribution of projected changes in the mean annual temperature (°C) from the reference period (1961–1990) to beginning-of-century (a, b: 2010–2039, top row), mid-century (c, d: 2040–2069, middle row), and end-of-century (e, f: 2070–2099, bottom row) under two emissions scenarios (columns), using the multimodel ensemble mean.

that the annual precipitation appears to decrease in Southwest China with respect to the 1961–1990 norm under RCP4.5. Moreover, this precipitation reduction is more pronounced under RCP8.5. The maxima for the annual precipitation decrease can reach 2–5% on the borders between Yunnan, Sichuan, Guizhou, and Guangxi Provinces under the RCP8.5 scenario. However, it should be noted that due to the lesser degree of agreement among the various GCM runs, the projected precipitation changes are subject to considerable uncertainty over Southwest China, although the multimodel ensemble mean shows a decrease in precipitation. In the mid-century, precipitation increases nationwide, and the magnitude of ΔP decreases from the inland regions in western and northern China, with a maximum value of 20–50%, toward southern and eastern China. In contrast to the period of 2010 to 2039, the climatological precipitation in the mid-century in Southwest China will increase by 2–5% under either the RCP4.5 or RCP8.5 scenario and is still characterized by a high level of uncertainty. In the end-of-century, the most noticeable feature is that the precipitation increase in northern and Northwest China is not as conspicuous as that in the mid-century. Overall, the dominant feature in the 21st century is the widespread precipitation increase over China.

6. Projected changes in climatological drought

The projected changes in climatological drought are first investigated from a national perspective. Each subplot in

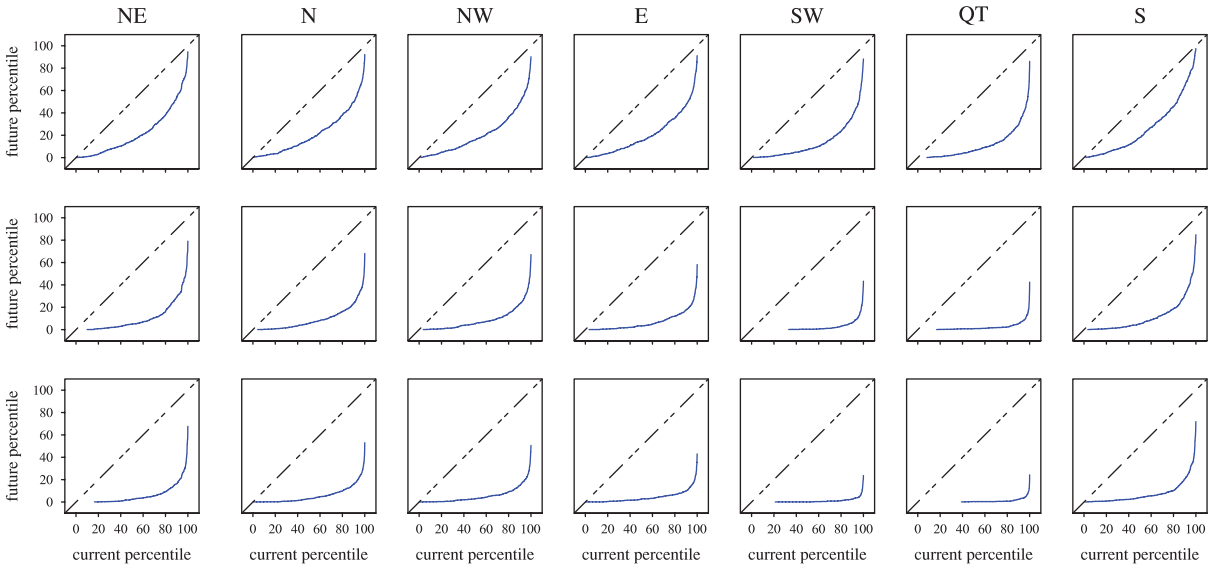

Figure 6. Relationship between percentiles of temperature in three future time periods (2010–2039, 2040–2069, and 2070–2099, y-axis) and the reference period (1961–1990, x-axis) for winter (December, January, and February). The December–February average temperature for seven climate divisions is first averaged to obtain the regional average winter temperature for a given model. A point on each subplot corresponds to one of the percentiles of the distribution in the reference period (x-coordinate) against the same percentile of the distribution in a future time period (y-coordinate). The percentiles of distribution are estimated from the empirical cumulative distribution function. If the distribution in the reference period remains unchanged in the future, the points in the percentile–percentile plot will lie roughly on the dash–dot line ($X = Y$).

Figure 9 shows the probability distribution of the PDSI as calculated across the whole country during a certain period under a given emission scenario. Specifically, each GCM contributes a portion, which equals number of grid cells multiplying total time steps, to the resulting histogram. It should be noted that no multimodel mean values are calculated prior to creating the probability distribution. There is no need to distinguish different seasons since the self-calibrating PDSI is a standardized measure of drought severity. As expected, the PDSI over the reference period has a near standard normal distribution due to the inherent property of the self-calibrating PDSI. The only asymmetry is that the frequency of incipient (or mild) drought is slightly greater than that of incipient wet (or slightly wet). It can be seen in Figure 9(a) that normal conditions are present 17% of the time and drought and wet occur 43 and 40% of the time, respectively. The frequencies of severe and extreme drought are reported as approximately 6.4 and 2.1%, respectively, while the frequencies of very wet and extremely wet are about 6.6 and 2.4%, respectively. In the beginning-of-century displayed in Figure 9(b) and (c), the central value of the histogram shifts from about 0.0 to the bin centred at −2.25 under both emissions scenarios, which means that drought that is considered moderate by current and historical standards will become the norm in the future. Besides the change in the mean, it should also be noted that the distribution is flattened to both the left and right, indicating increasing variance. Moreover, the peak frequency of the distribution decreases from 10 to 7%. Due to the shift of the distribution toward the left, the frequency of severe and extreme drought in current climate standards increases by 25%. However, the incidence of extreme wet conditions will rise rather than decrease, since the frequency of the PDSI (>5.0), which is nearly nonexistent in the reference period, will grow significantly to 2%. It can be concluded that the climate will become more extreme in the future under global warming. In addition, there is no significant dissimilarity between the probability distributions of PDSI under RCP4.5 and RCP8.5, because the p value derived directly from the resultant histograms (subplot (b) and (c) of Figure 9) by means of the Kolmogorov-Smirnov test (Corder and Foreman, 2009) is 0.99. Since the beginning-of-century, the apex of the histogram continues to shift to the left in both scenarios. It is evident that the distribution change is more pronounced under RCP8.5 than under RCP4.5, especially for the period 2070–2099. Under RCP8.5, drought that is classified as extreme according to current climate standards will become the norm in the end-of-century. Further inspection shows that the frequency of drought conditions (defined as PDSI < 0) is about 75% more than that of wet conditions (PDSI > 0) under RCP8.5. Though severe and extreme droughts become more probable in the future, there is still a high likelihood of very and extreme wet events. Though significant at the 95% confidence level, the p values obtained by the two-sample Kolmogorov-Smirnov test between the probability distributions under RCP4.5 and RCP8.5 are only 0.84 and 0.27 for the mid- and end-of-century respectively, indicating that the probability distributions of the PDSI under RCP4.5 and RCP8.5 begin to diverge since the mid-century.

A detailed evaluation of future climatological drought over China is illustrated in Figure 10. Generally, future droughts become more severe and widespread from the perspective of the PDSI. In the top panel of Figure 10, a

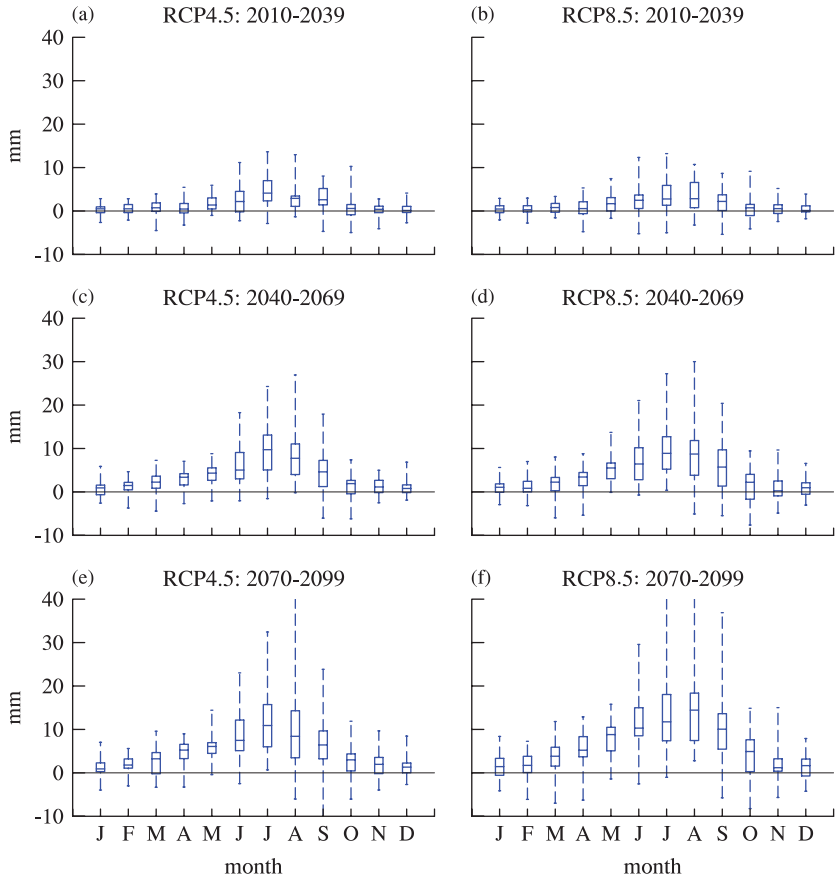

Figure 7. Projected changes in national average precipitation (mm month^{-1}) for each calendar month from the reference period (1961–1990) to (a, b: 2010–2039, top row), (c, d: 2040–2069, middle row), and (e, f: 2070–2099, bottom row) under two emissions scenarios (columns), showing all model results by means of boxplots. The band near the middle of the box shows the median and the bottom and top of the central rectangle spans the first quartile to the third quartile. Whiskers above and below the box show the location of the maximum and minimum.

noticeable feature is that the PDSI is generally projected to decrease in Southwest China, indicating the increasing risk of drought in that region. This phenomenon can be interpreted as the superimposition of increasing temperature and decreasing precipitation. Although the projected precipitation changes have great uncertainty, as shown by the disagreement of the multimodel results in Figure 8, various models indicate greater consensus on the PDSI decreases in most of Southwest China. As a consequence of intermodel consistency in projected temperature increases leading to increasing evaporation, the disagreement in projected precipitation change has been considerably damped in the calculation of the PDSI. Therefore, drying over Southwest China can be ascribed mainly to increasing evaporation, with higher temperatures resulting in an increasing tendency for drought in this region. In contrast, no drying tendency is found in northern China, in line with the projected increase in annual precipitation. Under RCP4.5, during the beginning of this century, as precipitation increases over North China while surface warming is relatively minimal, the PDSI remains unchanged or increases slightly, indicating no increase in drought risk. As time goes on, the PDSI continues to decrease over most of China. In the end-of-century, Southwest China and the Qinghai-Tibetan Plateau become considerably drier with the $\Delta PDSI$ reaching -4 to -5. This is also the case over other climate divisions, where the PDSI decreases by approximately 2. In spite of the overall projected increase in precipitation (Figure 8), the increase in drier land areas and drought severity can be attributed to increasing evaporation caused by surface warming. As a consequence, the mitigating effect of increasing precipitation on drought will be totally offset by rising temperatures.

Regional and seasonal discrepancies in the projected changes in drought are further revealed in Figure 11. An overall surface drying is evident, denoted by a decrease in the regional averaged PDSI. As can be seen from Figure 11, the regionally averaged PDSI decreases in the period 2010–2039 under RCP4.5 by approximately 1 (for NE, N, NW, E, and S) or 2–3 (for QT and SW), which is similar in magnitude to the decrease under RCP8.5. During this period, different scenarios have a limited effect on the change in climatological drought due to the analogous spatial distributions of temperature and precipitation changes between the two emissions scenarios, as shown in Figures 5 and 8.With respect to mid- and end-of-century as a whole, however, the regional averaged PDSI decreases about twice as much under RCP8.5 as under RCP4.5. Under RCP8.5, the aggravation of drought

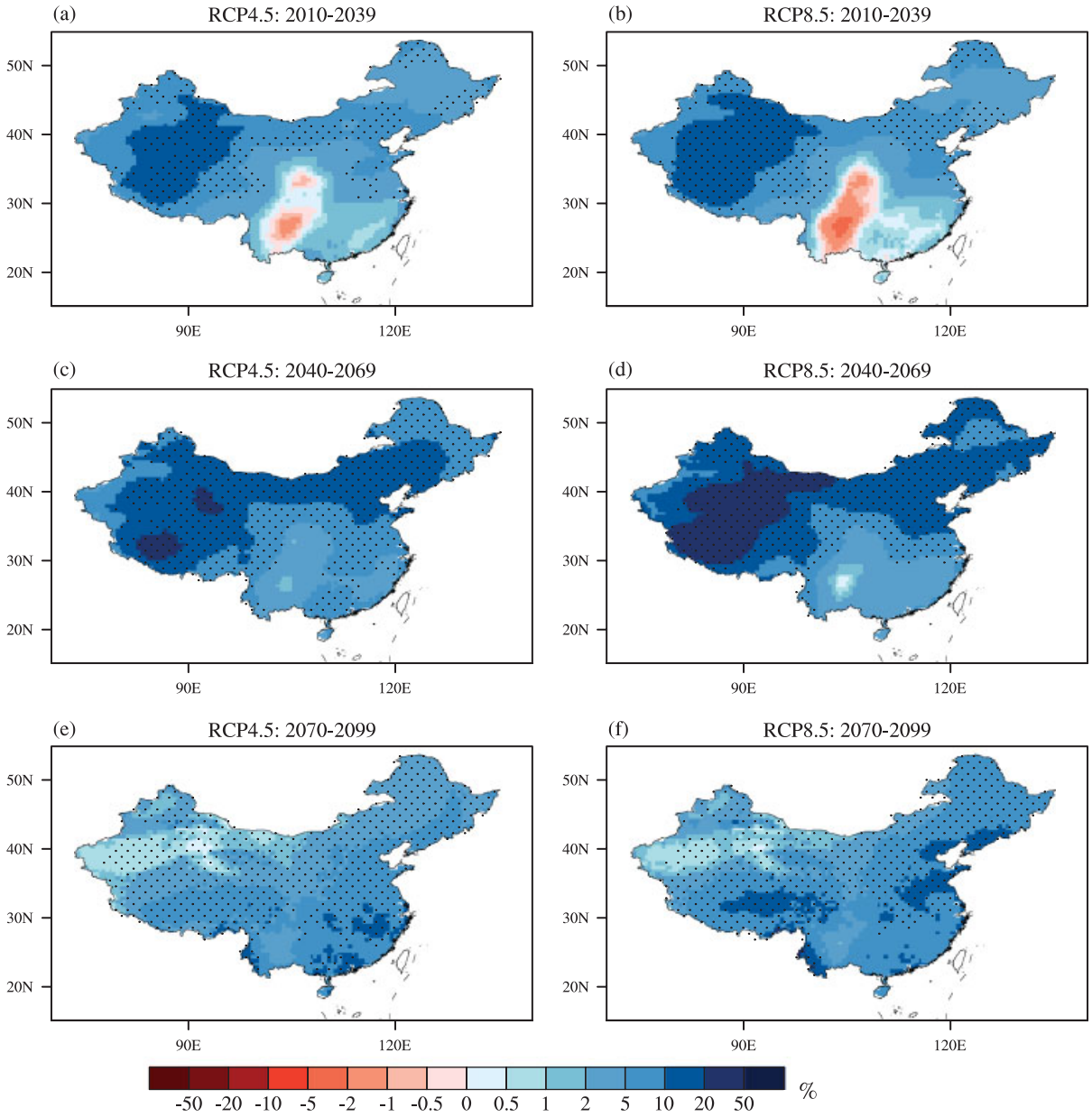

Figure 8. Geographic distribution of projected changes in the mean annual precipitation (%) from the reference period (1961–1990) to beginning-of-century (a, b: 2010–2039, top row), mid-century (c, d: 2040–2069, middle row) and end-of-century (e, f: 2070–2099, bottom row) under two emissions scenarios (columns), using the multimodel ensemble mean. These changes are plotted as a percentage relative to the 1961-1990 norm. The stippling indicates where 80% of the models agree at least on the sign of the mean change.

becomes more prominent in the end-of-century, compared with the situation under RCP4.5. The subplots for Southwest China and the Qinghai-Tibetan Plateau show that the regionally averaged PDSI is projected to decrease more sharply than in other climate regions of China, indicating these two climate zones may experience more severe drought. Consequently, advanced mitigation and adaptation measures are inevitable, especially in densely populated Southwest China.

Comparing each column of subplots in Figure 11 shows less evident seasonality even though the temperature and precipitation change has remarkable seasonality (Figures 4 and 7). We have also examined the spatial distribution of the PDSI changes in all four seasons and have found great consistency between different seasons (figure not shown). This seems contradictory because pronounced temperature increases and less significant precipitation increases in winter compared to summer should lead to more severe drought in winter. This is, however, the consequence of underlying nonlinear properties in the relationship between temperature and PET in the Thornthwaite equation. For a given temperature increase, the increase in PET is much more in summer than in winter due to the nonlinear dependence of PET on temperature. The plots in Figure 12 show the dependence of PET on temperature change. Since China ranges from roughly

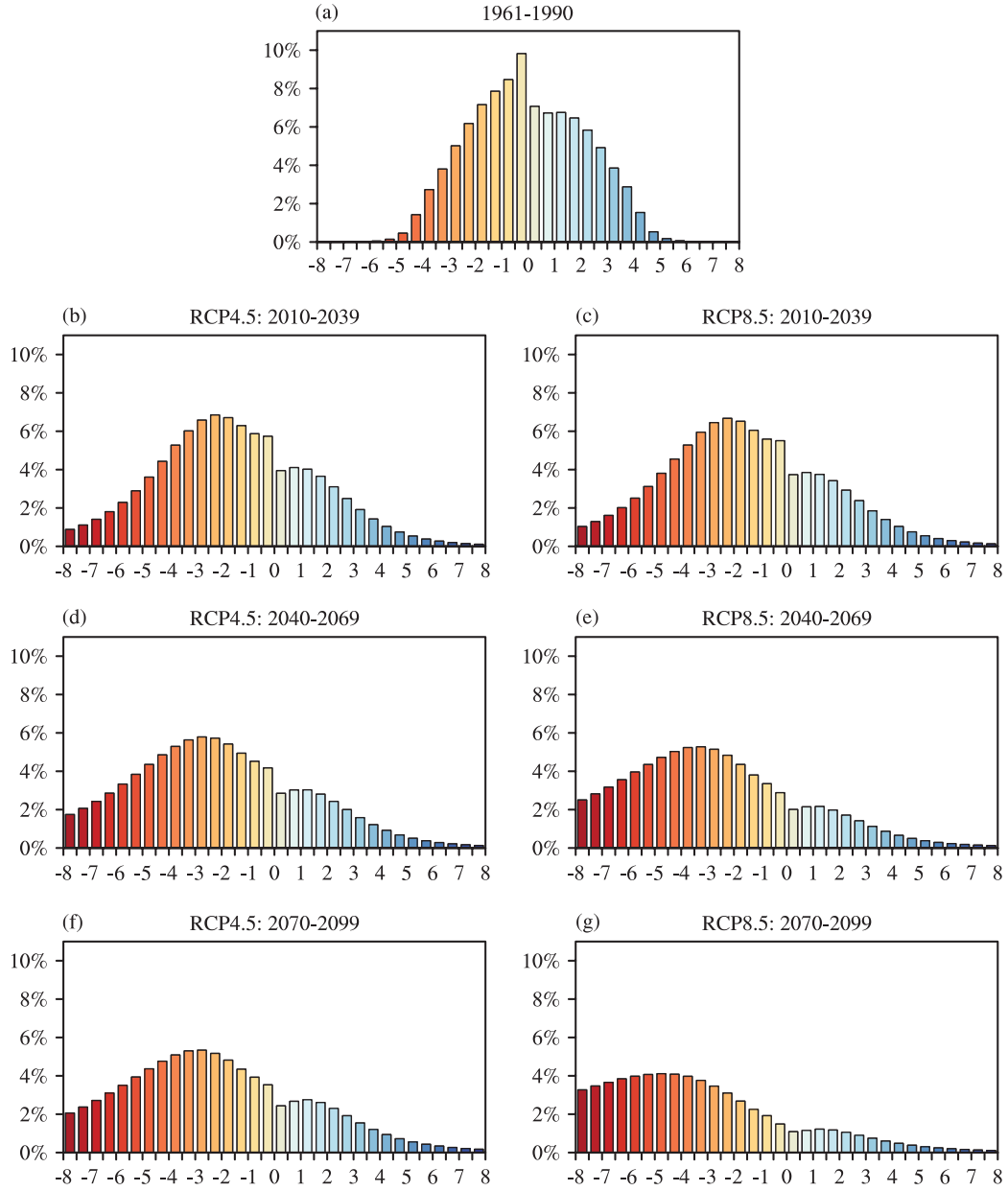

Figure 9. Probability distribution of the PDSI during (a) the reference period, (b) 2010–2039 under RCP4.5, (c) 2010–2039 under RCP8.5, (d) 2040–2069 under RCP4.5, (e) 2040–2069 under RCP8.5, (f) 2070–2099 under RCP4.5, and (g) 2070–2099 under RCP8.5. See text for further details.

20°N to 50°N and latitude is an important input into the PET calculation, four climate divisions that encompass this whole latitude range, namely Northeast China, North China, East China, and South China, are employed here to investigate the relationship between PET and temperature. The detailed procedure is to first add a given temperature increment (0, 1, 2, 4, and 6 °C, respectively) to each monthly climatological temperature and then apply the Thornthwaite equation to this newly established temperature series. In each subplot of PET versus month, the shapes of the curves are very similar, with a peak in July and a valley in winter. The most important point here is that the PET not only goes up each time in all calendar months when we raise the temperature, but it goes up much more in the summer months. If we raise the temperature by 2 °C for East China (Figure 12(c)), for instance, the PET will increase by 25.9 mm in July, but by only 1.9 mm in February. This means that the PET will rise much faster in summertime than in wintertime as temperature increases. In addition, the increasing rate of PET for a given temperature and month is comparatively high in the south and low in the north due to the temperature gradient from the south to the north in eastern China. The characteristics illustrated in Figure 12 can be interpreted as warm air absorbing more water vapour than cold air before saturation due to the relationship between vapour pressure and temperature.

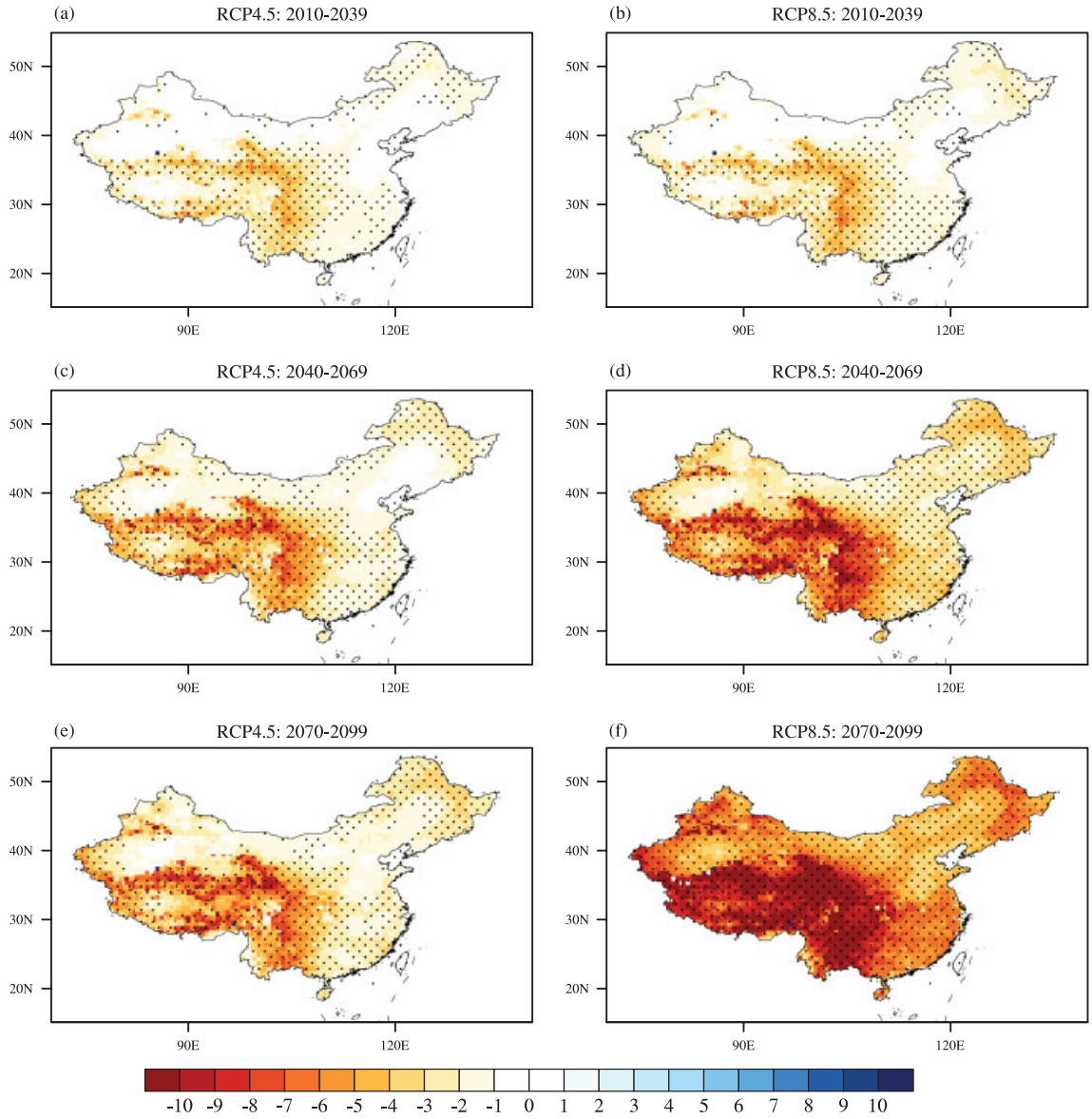

Figure 10. PDSI changes for three time periods: 2010–2039 (top row), 2040–2069 (middle row) and 2070–2099 (bottom row) with respect to the 1961–1990 norm under RCP4.5 (left column) and RCP8.5 (right column). The stippling indicates where 80% of the models agree at least on the sign of the mean change. Yellow to brown areas are projected to become drier.

In short, climatological droughts are predicted to be more severe in future, especially under RCP8.5 scenario. Such dramatic increases in drought conditions would lead to substantial impacts on agricultural, hydrological, and socioeconomic sectors and would present significant adaptation challenges.

7. Conclusions

The effects of climate change will be global in scope and will vary from region to region, with pronounced implications for China. China has the confluence of a huge population, insufficient arable land, and economic underdevelopment, which makes it vulnerable to climate change. Climate models, the most useful tools, are central to gauging future changes. However, global climate models are frequently characterized by coarse resolution and systematic error, which limit their direct application to regional-scale assessment and make future projections less reliable. Evaluation of model performances in China shows that the systematic errors in reproducing climatological temperature and precipitation as judged by MAE are 1.4–5.5 °C and 8.1–88.5 mm, depending on the calendar months and the outcomes from various climate models. Besides the climatological mean, large biases also exist in higher-order statistics including variance, skewness, and so on. Another issue is that the spatial resolution of GCMs is typically too coarse to assess regional climate change. As a result, to facilitate regional impact studies and to increase confidence in model projections, fine-resolution multimodel climate projections

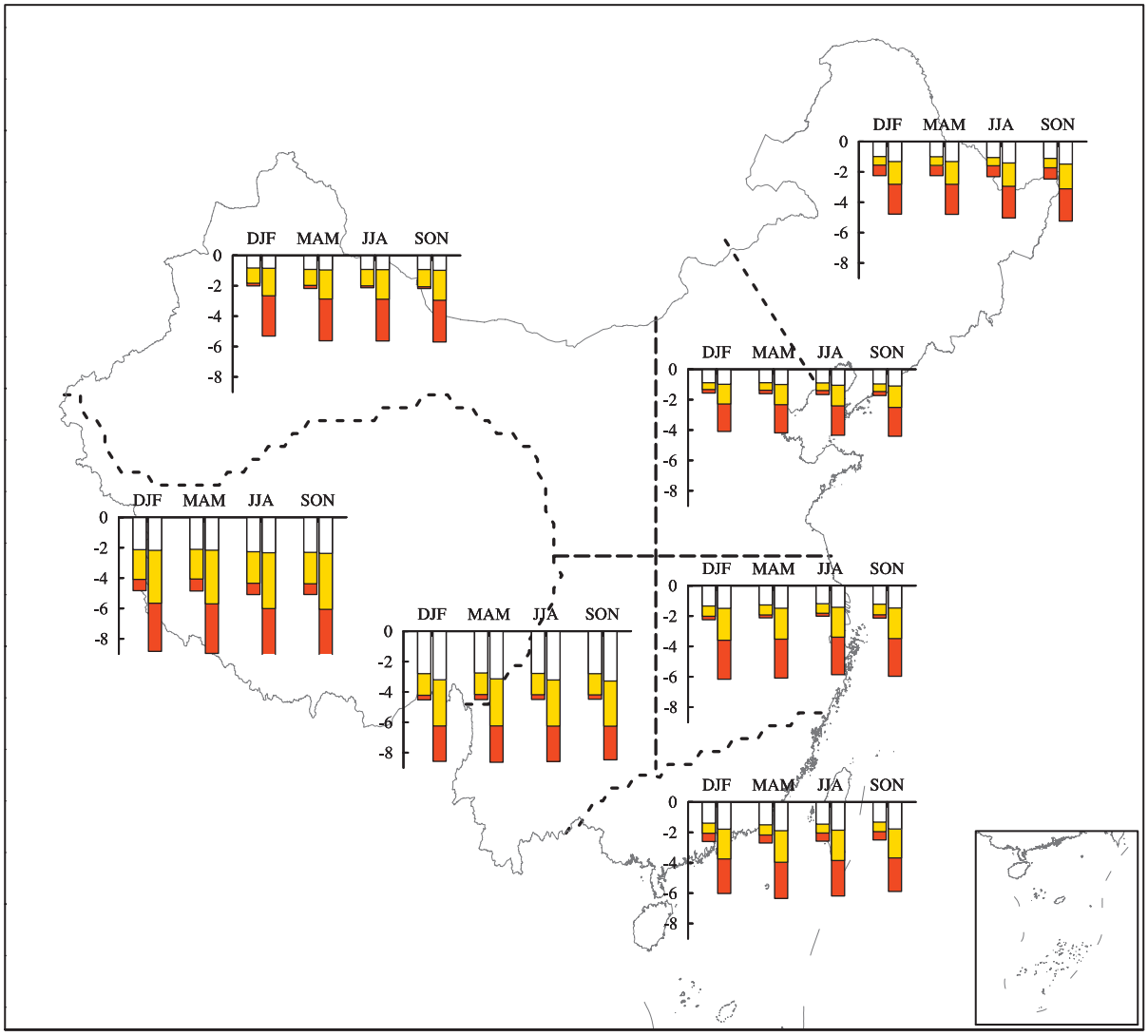

Figure 11. Seasonal PDSI changes in the seven climate divisions for three time slices (2010–2039, 2040–2069, and 2070–2099) under RCP4.5 and RCP8.5. The four columns comprising two bars arranged from left to right are the seasonal PDSI changes for winter (DJF), spring (MAM), summer (JJA), and autumn (SON). The two separate bars embedded within each column represent the changes under RCP4.5 and RCP8.5, respectively. Three colors (white, yellow, and orange) stand for PDSI changes for 2010–2039, 2040–2069, and 2070–2099, respectively.

over China are established based on 35 climate models and two emissions scenarios (RCP4.5 and RCP8.5) from CMIP5 by means of Bias Correction and Spatial Disaggregation (BCSD). Thanks to the bias correction procedure, the arithmetic mean is used in this study to build multimodel ensemble results instead of introducing a model weighting scheme. The main purpose of this study is to assess future changes in temperature, precipitation, and climatological drought over China based on this newly developed dataset to provide a framework for agricultural adaptation and water resource management in the future.

For temperature, the results suggest an increase in temperature over the whole country, with the largest increase occurring in the inland regions in winter. The yearly-averaged temperature is projected to increase by 0.8 to 1.6 °C (0.8 to 1.7 °C), 1.5 to 2.7 °C (2 to 3.7 °C) and 1.9 to 3.3 °C (3.4 to 6 °C) in three time slices (2010–2039, 2040–2069, and 2070–2099) under RCP4.5 (RCP8.5), respectively, in terms of multimodel ensemble results, depending on the subregions. In the beginning of the 21st century, the spatial patterns of temperature increase are substantially similar under RCP4.5 and RCP8.5, indicating the different emissions scenarios do not lead to significantly different temperature responses. Since the mid-century, however, the spatial distributions of temperature increase begin to diverge under different emissions scenarios, because the temperature increase is generally 2 °C more under RCP8.5 than under RCP4.5. Besides an increase in average temperatures nationwide, extreme low temperatures in winter also become less frequent, since the incidences of it defined as a seasonal temperature lower than the 9th percentile of the climatological distribution will sharply reduce to 0.1–1.7% under RCP4.5 for the period of 2010–2039 and even lower over the decades that followed. It is worth emphasizing that the

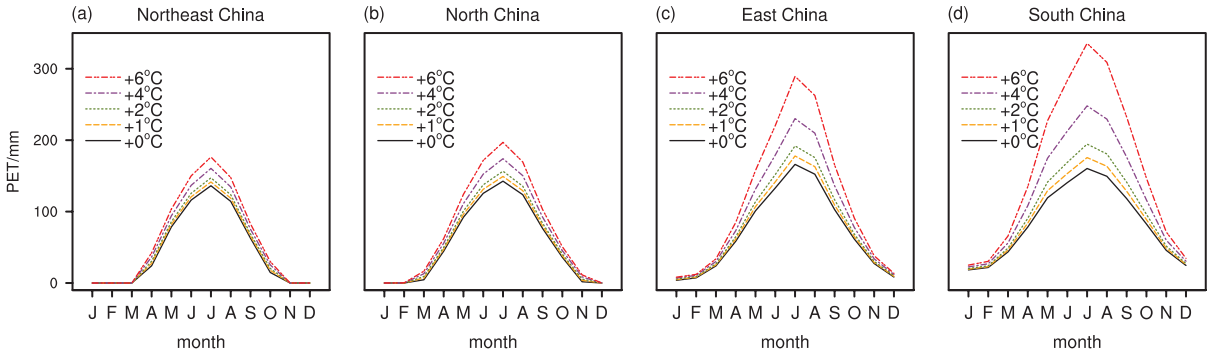

Figure 12. Monthly potential evapotranspiration as estimated by the Thornthwaite equation (x-axis: calendar month; y-axis: monthly potential evaporation, unit: mm month^{-1}) for (a) Northeast China, (b) North China, (c) East China, and (d) South China. 0 (black), 1 (orange), 2 (olive), 4 (orchid), and 6°C (red) is added to the climatological monthly temperature in all months and then the Thornthwaite equation is applied to the new established series.

decrease in the occurrence of extreme low winter temperatures in the future does not guarantee a decrease in extremely low temperatures on a daily scale; this needs to be further investigated by daily outputs from GCMs.

On the basis of the multimodel ensemble mean, northern China may receive more precipitation in the period of 2010–2039, and this pattern of precipitation increase will expand to the whole country. In the beginning-of-century, it is worth noting that the precipitation in Southwest China is projected to decrease, especially under RCP8.5, in spite of considerable inconsistency among different GCM runs. Compared with temperature, projected changes in precipitation are less certain, especially in southern China. Analogous to temperature changes, future precipitation changes will vary with the seasons, with the largest change in summer and the smallest in winter.

In spite of the projected precipitation increase, most areas of China will become drier as described by the PDSI. The rising temperature since the beginning of the 21st century, especially in the high-emission scenario, increases the atmospheric demand for moisture and plays an important role in increasing drought conditions, indicating that the increase in precipitation will be totally offset by surface warming. In both the beginning-of-century and the mid-century, increasing precipitation over Northwest China, North China, and Northeast China will alleviate the drying tendency yielded by surface warming. On the contrary, the joint effect of decreasing precipitation and warming will intensify the severity of drought in Southwest China. Furthermore, the severity of climatological drought will continue to increase for the rest of this century. The projected drying tendency for the period 2010–2039 shows scenario-independent geographical patterns. In contrast, drying is expected to be more severe under RCP8.5 than under RCP4.5 in the periods of 2040–2069 and 2070–2099. It is also worth noting that Southwest China is projected to experience more severe climatological drought in the future than any other part of China. Consequently, the environmental, ecological, and socioeconomic conditions in this region will be significantly affected by drought, and more efficient mitigation and adaptation strategies need to be carried out to address the impact of future droughts. The Sixth National Population Census of China in 2012 found the total population of Mainland China to be 1.3397 billion persons. If the drying actually occurs as indicated in Figures 10 and 11, a very large population will be severely affected in the coming decades.

Apart from temperature and precipitation responses on a monthly scale under global climate change, it is also important to focus on the change in extreme temperatures and precipitation on a daily scale. In addition, the frequency and duration of extreme drought, rather than the climatological drought presented in this study, will need to be further considered and examined.

Acknowledgements

The comments of two reviewers have led to a significant improvement of this paper. This work is supported by the National Natural Science Foundation of China Grants 41025017 and 41230527.

References

Allen RG, Smith M, Pereira LS, Perrier A. 1994. An update for the calculation of reference evapotranspiration. *Bull. Int. Comm. Irrig. Drain.* **43**: 35–92.

Alley WM. 1984. The Palmer Drought Severity Index: limitations and assumptions. *J. Clim. Appl. Meteorol.* **23**: 1100–1109, DOI: 10.1175/1520-0450(1984)023<1100:TPDSIL>2.0.CO;2

Chen W, Yang S, Huang R. 2005. Relationship between stationary planetary wave activity and the East Asian winter monsoon. *J. Geophys. Res.* **110**: D14110, DOI: 10.1029/2004JD005669

Chen W, Kang L, Wang D. 2006. The coupling relationship between summer rainfall in China and global sea surface temperature. *Clim. Environ. Res.* **11**: 259–269 (in Chinese).

Chen W, Gu L, Wei K, Huang R. 2008. Studies of the dynamical processes of East Asian monsoon system and the quasi-stationary planetary wave activities. *Chin. J. Atmos. Sci.* **32**: 950–966 (in Chinese).

Corder GW, Foreman DI. 2009. *Nonparametric Statistics for Non-Statisticians: A Step-By-Step Approach*. Wiley: Secaucus, NJ.

Dai A. 2011. Characteristics and trends in various forms of the Palmer Drought Severity Index during 1900–2008. *J. Geophys. Res.* **116**: D12115, DOI: 10.1029/2010JD015541

Feng L, Zhou T, Wu B, Li T, Luo J. 2011. Projection of future precipitation change over China with a high-resolution global atmospheric model. *Adv. Atmos. Sci.* **28**: 464–476, DOI: 10.1007/s00376-010-1016-x

Fowler HJ, Kilsby CG. 2007. Using regional climate model data to simulate historical and future river flows in northwest England. *Clim. Change* **80**: 337–367, DOI: 10.1007/s10584-006-9117-3

Furrer R, Sain SR, Nychka D, Meehl GA. 2007. Multivariate Bayesian analysis of atmosphere–ocean general circulation models. *Environ. Ecol. Stat.* **14**: 249–266, DOI: 10.1007/s10651-007-0018-z

Giorgi F, Mearns LO. 1991. Approaches to the simulation of regional climate change: a review. *Rev. Geophys.* **29**: 191–216, DOI: 10.1029/90RG02636

Giorgi F, Mearns LO. 2002. Calculation of average, uncertainty range, and reliability of regional climate changes from AOGCM simulations via the "reliability ensemble averaging'' (REA) method. *J. Clim.* **15**: 1141–1158, DOI: 10.1175/1520-0442(2002)015<1141:COAURA>2.0.CO;2

Gu W, Li C, Wang X, Zhou W, Li W. 2009. Linkage between Mei-yu Precipitation and North Atlantic SST on the decadal timescale. *Adv. Atmos. Sci.* **26**: 101–108, DOI: 10.1007/s00376-009-0101-5

Gudmundsson L, Bremnes JB, Haugen JE, Engen-Skaugen T. 2012. Technical note: downscaling RCM precipitation to the station scale using statistical transformations: a comparison of methods. *Hydrol. Earth Syst. Sci.* **16**: 3383–3390, DOI: 10.5194/hess-16-3383-2012

Hay LE, Wilby RL, Leavesley GH. 2000. A comparison of delta change and downscaled GCM scenarios for three mountainous basins in the United States. *J. Am. Water Resour. Assoc.* **36**: 387–397, DOI: 10.1111/j.1752-1688.2000.tb04276.x

Hobbins MT, Dai A, Roderick ML, Farquhar GD. 2008. Revisiting the parameterization of potential evaporation as a driver of long-term water balance trends. *Geophys. Res. Lett.* **35**: L12403, DOI: 10.1029/2008GL033840

Hu Z, Yang S, Wu R. 2003. Long-term climate variations in China and global warming signals. *J. Geophys. Res.* **108**: 4614, DOI: 10.1029/2003JD003651

Huang R, Zhou L, Chen W. 2003. The progresses of recent studies on the variabilities of the East Asian monsoon and their causes. *Adv. Atmos. Sci.* **20**: 55–69.

Kunkel KE, Liang XZ, Zhu J, Lin Y. 2006. Can CGCMs simulate the twentieth-century "warming hole" in the central United States? *J. Clim.* **19**: 4137–4153, DOI: 10.1175/JCLI3848.1

Li Y, Harrison SP, Zhao P, Ju J. 2009. Simulations of the impacts of dynamic vegetation on interannual and interdecadal variability of Asian summer monsoon with modern and mid-Holocene orbital forcings. *Glob. Planet. Change* **66**: 235–252.

Li H, Sheffield J, Wood EF. 2010a. Bias correction of monthly precipitation and temperature fields from Intergovernmental Panel on Climate Change AR4 models using equidistant quantile matching. *J. Geophys. Res.* **115**: D10101, DOI: 10.1029/2009JD012882

Li Q, Dong W, Li W, Gao X, Jones P, Kennedy J, Parker D. 2010b. Assessment of the uncertainties in temperature change in China during the last century. *Chin. Sci. Bull.* **55**: 1974–1982, DOI: 10.1007/s11434-010-3209-1

Li Y, Xiao Z, Ju J, Hu G. 2010c. The variations of dominant convection modes over Asia, Indian Ocean, and western Pacific Ocean during the summers of 1997-2004. *Adv. Atmos. Sci.* **27**: 901–920.

Liu Z. 2012. Comprehensive analysis of drought disasters in China from 1483 to 2010. *Diaster Adv.* **5**: 1275–1280.

Liu Y, Huang G, Huang R. 2011. Inter-decadal variability of summer rainfall in Eastern China detected by the Lepage test. *Theor. Appl. Climatol.* **106**: 481–488, DOI: 10.1007/s00704-011-0442-8

Ma Y, Chen W, Fong S, Leong K, Leong W. 2012. Interannual and interdecadal variations of precipitation over eastern China during Meiyu season and their relationships with the atmospheric circulation and SST. *Chin. J. Atmos. Sci.* **36**: 397–410 (in Chinese).

Maurer EP, Hidalgo HG. 2008. Utility of daily vs. monthly large-scale climate data: an intercomparison of two statistical downscaling methods. *Hydrol. Earth Syst Sci.* **12**: 551–563, DOI: 10.5194/hess-12-551-2008

Maurer EP, Brekke L, Pruitt T, Duffy PB. 2007. Fine-resolution climate projections enhance regional climate change impact studies. *EOS Trans. Am. Geophys. Union* **88**: 504, DOI: 10.1029/2007EO470006

Meehl GA, Covey C, Delworthc T, Latif M, McAvaney B, Mitchell JB, Stouffer R, Taylor K. 2007. The WCRP CMIP3 multimodel dataset: a new era in climate change research. *Bull. Am. Meteorol. Soc.* **88**: 1383–1394, DOI: 10.1175/BAMS-88-9-1383

Moss RH, Edmonds JA, Hibbard KA, Manning MR, Rose SK, van Vuuren DP, Carter TR, Emori S, Kainuma M, Kram T, Meehl GA, Mitchell JFB, Nakicenovic N, Riahi K, Smith SJ, Stouffer RJ, Thomson AM, Weyant JP, Wilbanks TJ. 2010. The next generation of scenarios for climate change research and assessment. *Nature* **463**: 747–756, DOI: 10.1038/nature08823

Palmer WC. 1965. *Meteorological Drought*. Research Paper No 45, US Dept of Commerce, 58.

Piani C, Haerter J, Coppola E. 2010. Statistical bias correction for daily precipitation in regional climate models over Europe. *Theor. Appl. Climatol.* **99**: 187–192, DOI: 10.1007/s00704-009-0134-9

Prudhomme C, Williamson J. 2013. Derivation of RCM-driven potential evapotranspiration for hydrological climate change impact analysis in Great Britain: a comparison of methods and associated uncertainty in future projections. *Hydrol. Earth Syst. Sci. Discuss.* **10**: 597–624, DOI: 10.5194/hessd-10-597-2013

Ren G, Xu M, Chu Z, Guo J, Li Q, Liu X, Wang Y. 2005. Changes of surface air temperature in China during 1951–2004. *Clim. Environ. Res.* **10**: 717–727 (in Chinese).

van der Schrier G, Jones PD, Briffa KR. 2011. The sensitivity of the PDSI to the Thornthwaite and Penman-Monteith parameterizations for potential evapotranspiration. *J. Geophys. Res.* **116**: D03106, DOI: 10.1029/2010JD015001

Seneviratne S, Nicholls N, Easterling D, Goodess C, Kanae S, Kossin J, Luo Y, Marengo J, McInnes K, Rahimi M. 2012. Changes in climate extremes and their impacts on the natural physical environment. In *Managing the Risks of Extreme Events and Disasters to Advance Climate Change Adaptation: A Special Report of Working Groups I and II of the Intergovernmental Panel on Climate Change (IPCC)*, Field CB, Barros V, Stocker TF, Qin D, Dokken DJ, Ebi KL, Mastrandrea MD, Mach KJ, Plattner G-K, Allen SK, Tignor M, Midgley PM (eds). Cambridge University Press: Cambridge, UK; 109–230.

Sharma D, Das Gupta A, Babel MS. 2007. Spatial disaggregation of bias-corrected GCM precipitation for improved hydrologic simulation: Ping River Basin, Thailand. *Hydrol. Earth Syst. Sci.* **11**: 1373–1390, DOI: 10.5194/hess-11-1373-2007

Shaw SB, Riha SJ. 2011. Assessing temperature-based PET equations under a changing climate in temperate, deciduous forests. *Hydrol. Process.* **25**: 1466–1478, DOI: 10.1002/hyp.7913

Solomon S, Qin D, Manning M, Chen Z, Marquis M, Averyt K, Tignor M, Miller H. 2007. *The Physical Sciences Basis*. Contribution of Working Group I to the Fourth Assessment Report of the Intergovernmental Panel on Climate Change. Cambridge University Press: Cambridge.

Taylor KE, Stouffer RJ, Meehl GA. 2012. An overview of CMIP5 and the experiment design. *Bull. Am. Meteorol. Soc.* **93**: 485–498, DOI: 10.1175/BAMS-D-11-00094.1

Thornthwaite CW. 1948. An approach toward a rational classification of climate. *Geogr. Rev.* **38**: 55–94.

Vidal J-P, Wade S. 2008a. A framework for developing high-resolution multi-model climate projections: 21st century scenarios for the UK. *Int. J. Climatol.* **28**: 843–858, DOI: 10.1002/joc.1593

Vidal J-P, Wade S. 2008b. Multimodel projections of catchment-scale precipitation regime. *J. Hydrol.* **353**: 143–158, DOI: 10.1016/j.jhydrol.2008.02.003

Vidal J-P, Wade S. 2009. A multimodel assessment of future climatological droughts in the United Kingdom. *Int. J. Climatol.* **29**: 2056–2071, DOI: 10.1002/joc.1843

Wang L, Chen W. 2013. Equiratio cumulative distribution function matching as an improvement to the equidistant approach in bias correction of precipitation. *Atmos. Sci. Let.*, DOI: 10.1002/asl2.454

Wang S, Li W. 2007. *Climate of China*. China Meteorological Press: Beijing.

Webb RS, Rosenzweig CE, Levine ER. 1993. Specifying land surface characteristics in general circulation models: soil profile data set and derived water-holding capacities. *Global Biogeochem. Cycles* **7**: 97–108.

Wei K, Chen W. 2011. An abrupt increase in the summer high temperature extreme days across China in the mid-1990s. *Adv. Atmos. Sci.* **28**: 1023–1029, DOI: 10.1007/s00376-010-0080-6

Wells N, Goddard S, Hayes MJ. 2004. A self-calibrating Palmer Drought Severity Index. *J. Clim.* **17**: 2335–2351, DOI: 10.1175/1520-0442(2004)017<2335:ASPDSI>2.0.CO;2

Widmann M, Bretherton CS, Salathé EP. 2003. Statistical precipitation downscaling over the northwestern United States using numerically simulated precipitation as a predictor. *J. Clim.* **16**: 799–816, DOI: 10.1175/1520-0442(2003)016<0799:SPDOTN>2.0.CO;2

Wilby RL, Wigley TML. 1997. Downscaling general circulation model output: a review of methods and limitations. *Prog. Phys. Geogr.* **21**: 530–548, DOI: 10.1177/030913339702100403

Willmott CJ, Matsuura K. 2005. Advantages of the mean absolute error (MAE) over the root mean square error (RMSE) in assessing average model performance. *Clim. Res.* **30**: 79–82, DOI: 10.3354/cr030079

WMO. 2007. The role of climate normals in a changing climate. World Climate Data and Monitoring Programme report WCDMP-No.61, WMO/TD No. 1377. World Meteorological Organization.

Wood AW, Maurer EP, Kumar A, Lettenmaier DP. 2002. Long-range experimental hydrologic forecasting for the eastern United States. *J. Geophys. Res.* **107**: 4429, DOI: 10.1029/2001JD000659

Wood AW, Leung LR, Sridhar V, Lettenmaier DP. 2004. Hydrologic implications of dynamical and statistical approaches to downscaling climate model outputs. *Clim. Change* **62**: 189–216, DOI: 10.1023/B:CLIM.0000013685.99609.9e

Wu R, Song Y, Wen Z, Huang G, Hu K. 2012. Interdecadal change in the relationship of southern China summer rainfall with tropical Indo-Pacific SST. *Theor. Appl. Climatol.* **108**: 119–133, DOI: 10.1007/s00704-011-0519-4

Xu C, Xu Y. 2012. The projection of temperature and precipitation over China under RCP scenarios using a CMIP5 multi-model ensemble. *Atmos. Oceanic Sci. Lett.* **5**: 527–533.

Zhang Y. 2012. Projections of 2.0°C warming over the globe and China under RCP4.5. *Atmos. Oceanic Sci. Lett.* **5**: 514–520.

Zhou T, Yu R. 2006. Twentieth-century surface air temperature over China and the globe simulated by coupled climate models. *J. Clim.* **19**: 5843–5858, DOI: 10.1175/JCLI3952.1

Zhou W, Li C, Chan JCL. 2006. The interdecadal variations of the summer monsoon rainfall over South China. *Meteorol. Atmos. Phys.* **93**: 165–175, DOI: 10.1007/S00703-006-0184-9

Zhou W, Li C, Wang X. 2007. Possible connection between Pacific oceanic interdecadal pathway and East Asian winter monsoon. *Geophys. Res. Lett.* **34**: L01701, DOI: 10.1029/2006GL027809

Zhou W, Chan JCL, Chen W, Ling J, Pinto JG, Shao Y. 2009. Synoptic-scale controls of persistent low temperature and icy weather over southern China in January 2008. *Mon. Weather Rev.* **137**: 3978–3991, DOI: 10.1175/2009MWR2952.1

Zhou B, Gu L, Ding Y, Shao L, Wu Z, Yang X, Li C, Li Z, Wang X, Cao Y, Zeng B, Yu M, Wang M, Wang S, Sun H, Duan A, An Y, Wang X, Kong W. 2010. The Great 2008 Chinese ice storm: its socioeconomic–ecological impact and sustainability lessons learned. *Bull. Am. Meteorol. Soc.* **92**: 47–60, DOI: 10.1175/2010BAMS2857.1

